

Coupled Numerical Modelling of Wind and Waves and the Theory of the Wave Boundary Layer

D. Chalikov · S. Rainchik

Received: 7 September 2009 / Accepted: 21 September 2010
© Springer Science+Business Media B.V. 2010

Abstract The description of a coupled wind and wave model in conformal coordinates is given. The wave model is based on potential equations for the flow with a free surface, extended with the algorithm of breaking dissipation. The wave boundary-layer (WBL) model is based on the Reynolds equations with the $K - \varepsilon$ closure scheme with the solutions for air and water matched through the interface. The structure of the WBL and vertical profiles of the wave-produced momentum flux (WPMF) in a long-term simulation of the coupled dynamics are investigated and parameterized. The shape of the β function connecting elevation and surface pressure is studied up to high nondimensional wave frequencies. The errors of a linear presentation of the surface pressure are estimated. The β function and the universal shape of the WPMF profile obtained in coupled simulations allow a formulation of the one-dimensional theory of the WBL, and the carrying out of a detailed study of the WBL structure including the dependence of the drag coefficient on the wind speed. It is shown that a wide scatter of the experimental data on the drag coefficient can be explained, taking into account the age of waves. It is suggested that a reduction of the drag coefficient at high wind speeds can be qualitatively explained by the high-frequency wave suppression.

Keywords Boundary layer · Numerical modelling · Sea waves · Wind–wave interaction

Electronic supplementary material The online version of this article (doi:[10.1007/s10546-010-9543-7](https://doi.org/10.1007/s10546-010-9543-7)) contains supplementary material, which is available to authorized users.

D. Chalikov
Faculty of Engineering and Industrial Sciences, Swinburne University of Technology, John Street,
Hawthorn, VIC 3122, Australia

D. Chalikov (✉)
P.P. Shirshov Institute of Oceanography, RAS, St. Petersburg Branch, 30, Pervaya Liniya, St. Petersburg,
Russia 199053
e-mail: dmitry-chalikov@yandex.ru

S. Rainchik
Russian State Hydrometeorological University, 98, Malookhtinsky Pr., St. Petersburg, Russia 195196
e-mail: srainchik@rshu.ru

1 Introduction

The wave boundary layer (WBL) is the lowest part of the atmospheric constant-flux layer (Chalikov 1976, 1978, 1986) where fluctuations produced by waves are clearly pronounced. The height of the WBL is of the order of a significant wave height H_s , normally a few metres. At the bottom it is in contact with the sea surface while at the top it merges with the atmospheric surface layer in which Monin–Obukhov similarity applies. In most cases the height of the WBL does not exceed the height of a dynamic sub-layer; hence, the direct influence of stratification on the wind–wave interaction is negligible. An indirect influence of stratification through the low-frequency part of the turbulent spectrum (gustiness) may be traced (Kahma and Calcoen 1992), and can be included into the WBL model using variable upper boundary conditions. Within the WBL the motion is profoundly influenced by the ocean surface waves, and since the WBL is responsible for wave drag, its structure changes the dynamics of the entire constant-flux layer. The total momentum flux τ splits in the WBL into two branches: the wave-produced momentum flux τ_w (WPMF) transferring energy and momentum to waves, and the shear turbulent flux generating currents. The contribution of the WPMF to the total flux is greatest at the wave surface, while the WPMF rapidly decreases with height within the WBL, eventually approaching zero at the top of the WBL where all of the momentum is transferred by shear turbulence.

Previous studies of the boundary layer above waves were based mostly on the conventional theory of a boundary layer above an infinite flat and rigid surface. In fact, the presence of waves was considered just as a kind of hindrance, and so the influence of waves was interpreted in terms of the roughness parameter only. No analysis of a wind profile close to the sea surface in the presence of the finite-amplitude waves has been suggested.

For the first time the dynamic interaction between waves and wind was qualitatively studied by the linear small-amplitude theories of Miles (1957) and Phillips (1977). These theories laid a solid foundation for the understanding of the wind and wave interaction mechanism provided by the surface pressure field; however, both actually ignored the presence of finite-amplitude disturbances.

A development of the numerical WBL models began in the 1970s with a simultaneous publication of several papers. Gent and Taylor (1976) studied a stationary air flow over a single wave for a broad range of wave and airflow parameters, and were the first to find a theoretical dependence of the wind–wave energy exchange on wave frequency. A very accurate WBL model based on the stream function was developed by Simonov (1982) whose most important result referred to the role of different turbulence closure schemes. He concluded that, for the typical magnitudes of the wave steepness, all of the closure schemes showed similar results. The notion of the fully non-linear modelling of wind–wave interaction (as well as the concept of the ‘WBL’) was first introduced by Chalikov (1976, 1978), where a fundamental problem of the derivation of the Reynolds equations for a boundary layer above the curvilinear moving surface was considered. He used a two-dimensional WBL model based on the finite-difference approximations in both directions, with all calculations performed either for a monochromatic wave field or just for several wave modes (Chalikov 1986). Development of an accurate numerical method for the solution of the general elliptic equation for the pressure above a non-stationary multimodal surface presented the most difficult computational problem. The main results obtained with the use of the old version of the model are as follows:

- (1) The Reynolds equations in a surface-following coordinate system as well as a general formulation of the WBL problem were derived.

- (2) The spectral shape of the wind–wave interaction parameter (β function) was found with the pre-assigned angular distribution based on the “apparent” frequency. The statistical structure of the WBL (including profiles and spectral composition of the first, second and some of the third moments of the wave-produced pressure, velocities and turbulence) was studied.
- (3) One-dimensional theory of the WBL considering the spectral structure of wave-produced momentum fluxes (Chalikov and Belevich 1993; Chalikov 1995) was developed.
- (4) New energy input and dissipation schemes (Tolman and Chalikov 1994, 1996) in the NWS operational wave forecast *WAVEWATCH* model (see the website <http://polar.wmb.noaa.gov/waves>) were implemented. The energy input formulation is more accurate than that used in the wave model (WAM). The comparison of wave forecasts produced by the *WAVEWATCH* III (Version 1.15) and the WAM (Cycle 4) models using buoy and satellite data has clearly shown that the *WAVEWATCH* model has some advantages, as compared with the WAM model.

The results of further numerical modelling (Chalikov 2005) showed that the term “very small amplitude” is more appropriate than “small amplitude” since, even for the steepness of the order of 0.05, the non-linearity becomes an essential property of the wave dynamics. Also note that applicability of the single-mode linear analysis for real finite-amplitude multimodal wave fields was never seriously discussed. What makes this problem special is the necessity of using a surface-following coordinate system for derivation of correct non-linear equations. After transformation the dynamic equations become highly complex and difficult to integrate, however, they allow the essence of the process to be described, i.e. the interaction of a turbulent wind with finite-amplitude waves.

The wind–wave interaction mechanism has been comprehensively studied within the framework of the ocean wave evolution problem. All of the studies were focused on the parameterization of the so-called input and dissipation source terms in the wave prediction models. Even for such processes the existing theories seem to be either highly simplified (e.g., the Miles’ quasi-linear wind input theory) or purely speculative, as in the case of the wave energy dissipation due to whitecapping. Moreover, it is a bare reality that the frequently cited Hasselmann (1962) approach to the calculation of a non-linear interaction was never used in wave forecasting models due to its high complexity. Furthermore, direct observations of a number of characteristics are hardly possible. An indirect analysis based on observations of the spectrum evolution is unable to separate the input, dissipation and non-linear interaction effects.

A standard spectral description of the energy input to waves is based on a concept of the linear superposition of fluxes to spectral components calculated according to the Miles’ theory. This principle is incorrect for steep waves. All the previous models considered an air flow above the single harmonic wave and suggested steadiness of the flow (see, for example, Janssen 1991). Actually, this assumption is acceptable only for small-amplitude waves. Due to a strong non-linearity (leading to the formation of bound waves, focusing of the energy in a physical space, and wave breaking), the wave field cannot be represented as a superposition of linear waves with random phases. The dynamic wind–wave interaction is highly complex. For example, long waves modify local drag, which influences the energy input to short waves, while the short waves produce a local drag that influences the flow over large waves. In general, all waves ‘spring, burgeon and fall’ in the environment created by the entire spectrum. The energy input to waves, even with moderate steepness, is rather concentrated in physical space than in Fourier space. Hence, a Fourier image of the input is often difficult to interpret.

The more comprehensive theoretical formulation of the coupled problem became possible after introduction of the unsteady surface-following conformal mapping (Chalikov and

[Sheinin 1996, 1998](#)). The new method used for the direct wave modelling was successfully validated and showed very high accuracy. The method was used for investigation of the potential wave dynamics, such as the wavenumber/frequency two-dimensional (2-D) spectrum ([Chalikov and Sheinin 1996, 1998](#)), shallow water-wave dynamics ([Sheinin and Chalikov 2005](#)), steep wave dynamics ([Chalikov and Sheinin 2005](#)), the statistical properties of waves ([Chalikov 2005](#)), the Benjamin–Feir instability ([Chalikov 2009](#)) and freak wave dynamics ([Chalikov 2009](#)). After transformation to conformal coordinates the one-dimensional (1-D) equations obtain quite a simple form. The model is so precise that any comparison with observations allows judging rather of the 1-D potential approach applicability to the real process than of the accuracy of the model itself.

The numerical hydrodynamic modelling is similar to ideal laboratory modelling (no scale limitation, wide parameter ranges, and the availability of simple ‘observations’ of any characteristics in any location); however, the applicability depends on the efficiency of the theoretical assumptions used. Numerical modelling provides more detailed data than a physical simulation. Such a situation is typical in other branches of fluid dynamics (perhaps better developed), especially in technical fluid mechanics. It has been proved that numerical methods really do provide high quality results that can be combined with those obtained from the experiments.

Thus, the motivations for the development of a new approach are quite obvious. It is impossible to prove that co-existing waves interact with the atmosphere as a set of independent waves, whilst the integral result can be obtained by a simple superposition of monochromatic cases. It is well known that even a single wave produces a broad spectrum of pressure fluctuations, which modifies the flow. The first attempt to consider non-linearity and group effects was made with the use of a finite-difference model (see [Chalikov 1986](#)), where the wave surface was assigned as a superposition of running waves with different frequencies. This approach is much closer to reality than that based on a stationary single-mode model. However, it was found that such an approach, being more precise (and more complicated) than the monochromatic stationary approach, turned out to be also imperfect due to two reasons: (1) the peculiar wave shapes and the non-linear group structure are not represented in the above model; (2) the finite-difference model cannot provide the required accuracy.

The most reliable approach for the study of the wind–wave interaction problem involves modelling of the coupled wave and the WBL dynamics ([Chalikov 1998](#)). The spectral approach to this problem is quite suitable; however, it should be used as a method for a numerical solution of the equations, and for presentation of the results. The most complicated processes, such as group effects, wave breaking, bound waves and the development of extreme waves occur in physical space; hence, the spectral image of the above processes is often not representative.

It is quite obvious that real waves have more or less sharp crests and smooth troughs. At the same time, the Stokes waves are the exact solution of the full equations. The Stokes waves are stable in the absence of disturbances, while they slowly transform as a result of the [Benjamin and Feir \(1967\)](#) instability in the presence of disturbances. However, harmonic waves quickly disintegrate and obtain the shape of the Stokes waves even in the absence of disturbances. The wave field always includes the so-called ‘bound waves’ whose phase speed is equal to that of a carrying wave. The term “bound waves” is quite vague as it obscures the genuine nature of the phenomenon. Actually, large waves are non-linear phenomena that are more or less stable and consist of a great number of linear modes with the nearly constant amplitudes and fixed phases. As a result, the multi-mode wave field is rather approximated by the superposition of non-linear modes (the Stokes waves) than by the superposition of linear modes with random phases ([Chalikov 2005](#)). Such properties of real waves are closely connected with

the problem of wind and wave interaction. This problem of geophysical fluid dynamics has always been the object of broad investigations; however, the majority of studies was based on the small-amplitude assumption, though it was never discussed which amplitudes may be considered small. Numerous analytical studies (based on the simplified equations) that followed Miles (1957) actually did not lead to a deeper understanding of the problem. The structure of the flow and a wave-produced drag above the sharp-crested waves differ from those for the harmonic waves. A more realistic approach is based on numerical modelling of a stationary flow above a wavy surface (represented by one mode). Such models based on the Reynolds equations and turbulent closure schemes (Gent and Taylor 1976; Chalikov 1978) were used for investigation of the structure of a boundary layer above the finite-amplitude harmonic waves (see Chalikov 1986). The results obtained with the use of such models are definitely closer to reality than the results of analytical exercises, though they are also imperfect. Despite the fact that Chalikov’s model has undergone numerous modifications (see, for example, Mastenbroek et al. 1996), it remained hardly suitable for investigation of the real process. Moreover, this scheme was based on the finite-difference approach, while for the periodic-wave problem it would be more appropriate to use the Fourier-transform method. The pressure field was calculated through the solution of the finite-difference Poisson equation, which imposes tough limitations on the wave steepness. The first attempts to consider more than one harmonic mode were also not quite successful.

The current approach to the problem (Chalikov 1998) is based on several new principles: (1) the model is formulated as a high-resolution spectral problem in a non-stationary surface-following coordinate system, (2) waves are the object of modelling: the full potential wave equations are solved along with the equations for the boundary layer with matching of the solutions on the interface, (3) a well-developed and powerful Fourier-transform method is used.

It is obvious that even minor obstacles (such as sharpening of a crest) produce a dramatic change in the pressure field and form drag (this effect is well known in engineering fluid mechanics). It is also well-known that just a simple group effect can produce high and steep waves (in physical space) with a deep minimum of the pressure behind the crests. Non-linearity enhances the effect of sharpening, thus strongly increasing the pressure anomalies. On the whole, the wave drag and the energy exchange are the result of the ensemble effect of non-stationary fluctuations of pressure and surface stresses. It is clear that all such processes are completely absent in monochromatic stationary models.

2 Equations of the WBL

It is impossible to provide an exact formulation of the 2-D wind–wave interaction problem without introduction of the surface-following conformal coordinates. A consistent development of the approach to the problem of wind–wave interaction began with Chalikov (1976, 1978). Let us consider a boundary layer above a curved periodic surface $\eta(x, t)$, and whose shape is represented by the Fourier expansion:

$$\eta(x, t) = \sum_{-M}^M h_k(t) \vartheta_k(x), \tag{1}$$

where h_k is amplitude, M is a truncation number, and $\vartheta_k(x)$ denotes the following function:

$$\vartheta_k(\xi) = \begin{cases} \cos(k\xi) & k \geq 0 \\ \sin(k\xi) & k < 0 \end{cases}, \tag{2}$$

noting that $(\vartheta_k)_\xi = k\vartheta_{-k}$, and $\sum (A_k\vartheta_k)_\xi = -\sum kA_{-k}\vartheta_k$. Let us introduce the conformal surface-following coordinate transformation for the domain $(0 < x \leq 2\pi, H_w < z < H_a)$ (Chalikov and Sheinin 1996, 1998):

$$x = \xi \mp \sum_{-M \leq k \leq M, k \neq 0} \eta_{-k}(\tau) \frac{\cosh k([H_a, H_w] \mp \zeta)}{\sinh k[H_a, H_w]} \vartheta_k(\xi), \tag{3a}$$

$$z = \xi + \sum_{-M \leq k \leq M, k \neq 0} \eta_{-k}(\tau) \frac{\sinh k([H_a, H_w] \mp \zeta)}{\sinh k[H_a, H_w]} \vartheta_k(\xi), \tag{3b}$$

$$t = \tau, \tag{3c}$$

where H_a is the WBL height, and $-H_w$ is the water domain depth. The top signs in Eq. 3a,b refer to the air domain, while the bottom signs refer to the water domain. Note that the transformation (3a,b) is non-linear, since $\vartheta_k(\xi)$ are functions of the new coordinate ξ . At $\zeta = 0$ function $z(\xi)$ describes the wave surface:

$$z(\xi, 0, \tau) = \eta(\xi, \tau) = \sum_{-M}^M \eta_k(\tau) \vartheta_k(\xi), \tag{4}$$

where M is the assigned number of modes while η_k are the Fourier coefficients in a curvilinear coordinate system. Those coefficients differ from the Fourier coefficients h_k for the water surface in the Cartesian coordinate system. To obtain the same accuracy of approximation of the surface η the number of modes in the Cartesian coordinates should be less than in the lower coordinates and more than in the upper coordinates.

The governing equations are obtained by averaging the Navier–Stokes equations, but in the presence of a moving 2-D interface averaging is not a simple problem; Phillips (1977) discussed this problem in detail (see also Chalikov 1978). However, it should be pointed out that averaging of the equations for the 3-D case is always connected with some ‘a priori’ simplifications, so it cannot be done formally as was done for a quasi-stationary flow in a simple domain (Monin and Yaglom 1971). Obviously, the best way to avoid some of the simplifications is usage of the large-eddy simulation (LES) technique. Above the 1-D surface averaging can be understood as averaging along $y = constant$ (Phillips 1977).

After transformation into the new coordinate system and averaging (discussion of an averaging procedure in the presence of a curvilinear surface was given by Chalikov (1978)), the Euler equations can be written as follows (the sign of averaging for the first-order moments is omitted):

$$\frac{dJu}{d\tau} = -\frac{\partial px_\xi}{\partial \xi} + \frac{\partial pz_\xi}{\partial \zeta} - \frac{\partial (x_\xi \overline{u'u'} + z_\xi \overline{u'w'})}{\partial \xi} - \frac{\partial (-z_\xi \overline{u'u'} + x_\xi \overline{u'w'})}{\partial \zeta}, \tag{5a}$$

$$\frac{dJw}{d\tau} = -\frac{\partial pz_\xi}{\partial \xi} - \frac{\partial px_\xi}{\partial \zeta} - \frac{\partial (x_\xi \overline{u'w'} + z_\xi \overline{w'w'})}{\partial \xi} - \frac{\partial (-z_\xi \overline{u'w'} + x_\xi \overline{w'w'})}{\partial \zeta}, \tag{5b}$$

where p is a deviation from the hydrostatic pressure normalized by air density, x_ξ and z_ξ are metric coefficients, J is the Jacobian of mapping

$$J = x_\xi^2 + z_\xi^2, \tag{6}$$

and $d/d\tau$ denotes a full derivative on time,

$$\frac{dJ()}{d\tau} = \frac{\partial J()}{\partial \tau} + \frac{\partial JU()}{\partial \xi} + \frac{\partial JW()}{\partial \zeta}, \tag{7}$$

where U, W are contravariant velocity components

$$U = J^{-1} ((u - x_\tau) x_\xi + (w - z_\tau) z_\xi), \tag{8a}$$

$$W = J^{-1} (-(u - x_\tau) z_\xi + (w - z_\tau) x_\xi). \tag{8b}$$

The continuity equation takes the form:

$$\frac{\partial \tilde{u}}{\partial \xi} + \frac{\partial \tilde{w}}{\partial \zeta} = 0, \tag{9}$$

where \tilde{u} and \tilde{w} are covariant velocity components:

$$\tilde{u} = ux_\xi + wz_\xi, \tag{10a}$$

$$\tilde{w} = -uz_\xi + wx_\xi. \tag{10b}$$

While approaching the surface the 'vertical' velocity W tends to zero, and the kinematic condition $W = 0$ becomes valid with increasing accuracy. On the surface itself $W = 0$ strictly, and $u = u_0, w = w_0$, where u_0 and w_0 are the surface velocity components. The fact that $W = 0$ implies that the momentum and any substance are not transferred by velocity through the interface. To derive Eqs. 2–9 the following properties of conformal mapping were used:

$$x_\xi = z_\zeta, \quad x_\zeta = -z_\xi, \quad x_\xi = J^{-1} \xi_x, \quad x_\zeta = -J^{-1} \xi_z. \tag{11}$$

The second- and third-order moments, containing fluctuations of metric coefficients and the Jacobian, are omitted, since such subgrid moments rapidly attenuate with increase of distance from the surface (see a discussion of this problem in Chalikov 1978). The second-order turbulence moments are represented as a product of the turbulent viscosity coefficient K_m , and the corresponding component of the velocity strain tensor Φ_{ij} (Monin and Yaglom 1971). The coefficient K_m is taken in the form:

$$K_m = c_k e^2 / \varepsilon, \tag{12}$$

($K - \varepsilon$ model), where e is the kinetic energy of turbulence, ε is the rate of dissipation of e (Launder and Spalding 1974), $c_k = 0.0073$, and

$$\overline{u'u'} = 2K_m J^{-1} \Phi_{11} = 2K_m J^{-1} \left(\frac{\partial ux_\xi}{\partial \xi} - \frac{\partial uz_\xi}{\partial \zeta} \right) + \frac{2}{3} e, \tag{13a}$$

$$\overline{u'w'} = K_m J^{-1} \Phi_{12} = K_m J^{-1} \left(\frac{\partial (uz_\xi + wx_\xi)}{\partial \xi} - \frac{\partial (ux_\xi - wz_\xi)}{\partial \zeta} \right) \tag{13b}$$

$$\overline{w'w'} = 2K_m J^{-1} \Phi_{22} = 2K_m J^{-1} \left(\frac{\partial wz_\xi}{\partial \xi} - \frac{\partial wx_\xi}{\partial \zeta} \right) + \frac{2}{3} e. \tag{13c}$$

At the upper bound the metric coefficients obtain the values: $z_\xi = 0$ and $x_\xi = 1$, hence, the boundary conditions take the following form:

$$z = \zeta = H_a; \overline{u'w'} = \tau, \quad w = 0, \tag{14}$$

where τ is the vertical flux of the horizontal momentum beyond the WBL (an outer stress). The tangential turbulent stress on the surface τ_0 is calculated with use of the quadratic law:

$$\tau_0 = C_l |\tilde{u}_1 - \tilde{u}_0| (\tilde{u}_1 - \tilde{u}_0). \tag{15}$$

Here \tilde{u}_1 and \tilde{u}_0 are covariant components of the velocity in the lowest layer and on the interface, respectively, C_l is the local drag coefficient, the definition of which is given below.

The evolution of e and ε is described by

$$\frac{dJe}{d\tau} = \frac{\partial}{\partial \xi} K_e \frac{\partial e}{\partial \xi} + \frac{\partial}{\partial \zeta} K_e \frac{\partial e}{\partial \zeta} + P - \varepsilon, \tag{16a}$$

$$\frac{dJ\varepsilon}{d\tau} = \frac{\partial}{\partial \xi} K_\varepsilon \frac{\partial \varepsilon}{\partial \xi} + \frac{\partial}{\partial \zeta} K_\varepsilon \frac{\partial \varepsilon}{\partial \zeta} + \frac{\varepsilon}{e} (c_2 P - c_4 \varepsilon), \tag{16b}$$

where the diffusion coefficients K_e and K_ε are proportional to the coefficient of the turbulent viscosity $K_e = K_m/c_e$, $K_\varepsilon = K_m/c_\varepsilon$, while P is a rate of turbulent energy production:

$$P = 0.5JK_m (\Phi_{11}^2 + 2\Phi_{12}^2 + \Phi_{22}^2). \tag{17}$$

The rate of production P_H at the upper boundary of the domain $z = \zeta = H_a$ is calculated through

$$P_H = \frac{v_*^3}{\kappa H_a}, \tag{18}$$

where $v_* = \tau^{1/2}$ is a friction velocity at $z = H_a$, and the energy of turbulence e and the rate of dissipation ε are given by

$$e_H = c_1 v_*^2, \tag{19a}$$

$$\varepsilon_H = \frac{v_*^3}{\kappa H_a}. \tag{19b}$$

The vertical diffusion of the turbulent energy normal to the surface $\zeta = 0$, as well as the diffusion $K_e \frac{\partial e}{\partial \zeta}$ at the upper bound $\zeta = H_a$, are both equal to zero. The vertical diffusion of the dissipation rate normal to the surface $\zeta = 0$ and that at the upper bound $\zeta = H_a$ are equal to:

$$K_\varepsilon \frac{\partial \varepsilon}{\partial \zeta} (\zeta = 0) = -v_{s0}^4 z_1^{-1} c_3^{-1}, \tag{20a}$$

$$K_\varepsilon \frac{\partial \varepsilon}{\partial \zeta} (\zeta = 0) = -v_{s0}^4 z_1^{-1} c_3^{-1} \tag{20b}$$

respectively, where $v_{s0} = \tau_0^{1/2}$ is the local tangential friction velocity defined by the local turbulent tangential stress τ_0 on the interface. The closure scheme based on Eqs. 13–17 uses a set of the empirical constants: $\kappa \approx 0.41$ (the Karman constant), $c_1 = 3.7$, $c_e = 1$, $c_2 = 1.92$, $c_3 = 1.3$. In the absence of waves, as follows from the self-similarity of a logarithmic boundary layer, the constant c_4 is connected with other constants through

$$c_4 = (c_1 - c_2) \kappa^{-2} c_3^{-1}. \tag{21}$$

All the equations have been written in a non-dimensional form based on the following scales: length L ($2\pi L$ is a horizontal size of the domain) and g is the acceleration due to gravity. All other scales have been constructed with the use of g and L .

3 The Numerical Scheme for the WBL Equations

The numerical scheme is based on the Fourier-transform method (Orszag 1970) and on the fast Fourier transform for an arbitrary number of modes. A detailed description of the method applied to the wave modelling problem is given in Chalikov and Sheinin (1998).

The core of the method is that the linear part of the equation is approximated directly, while the products of variables are calculated on a uniform ξ -coordinate grid with a number of knots $N = 4M$ (M is the number of the Fourier modes). Then, the Fourier coefficients of the products are used for integration in time or for the calculation of derivatives over the ‘vertical’ coordinate ζ . The derivatives over ξ are calculated through analytical differentiation of the Fourier series. The vertical operators are approximated on a stretched grid where intervals between the knots $\Delta\zeta_j$ are calculated with the use of the relation $\Delta\zeta_{j+1} = \gamma\Delta\zeta_j$ (γ is a stretching coefficient; the index j increases), and the first value of $\Delta\zeta(j = 1)$ is defined from the following condition:

$$\sum_{j=1}^K \Delta z_k = H_a, \tag{22}$$

where K is the total number of levels in the WBL. To improve the accuracy of the finite-difference approximation for the zero-number modes of u and ε , it was taken into account that:

$$u \propto \ln(\zeta) + const, \tag{23a}$$

$$\varepsilon \propto \zeta^{-1}, \tag{23b}$$

For integration in time the fourth-order Runge–Kutta scheme was used.

The most difficult problem arising while solving the fluid mechanics equations in curvilinear coordinates is calculation of a pressure field that provides the continuity condition (9). It is well-known that the solution quickly becomes unstable if the equation of continuity does not yield high accuracy. The dynamical equations for covariant components of the velocity (10) do not take the following form:

$$\frac{\partial \tilde{u}}{\partial \tau} = -\frac{\partial p}{\partial \xi} + \tilde{F}_u, \tag{24a}$$

$$\frac{\partial \tilde{w}}{\partial \tau} = -\frac{\partial p}{\partial \zeta} + \tilde{F}_w, \tag{24b}$$

where F_u and F_w are straightforward designations of the sum of turbulent and convective terms calculated as a combination of the right-hand sides of Eqs. 5a,b at each sub-step of the Runge–Kutta scheme. Equations 24a,b gives a possibility to derive a standard form of the Poisson equation for the updated pressure p^l

$$\frac{\partial^2 p^l}{\partial \xi^2} + \frac{\partial^2 p^l}{\partial \zeta^2} = \frac{1}{\Delta t} \left(\frac{\partial \tilde{u}}{\partial \xi} + \frac{\partial \tilde{w}}{\partial \zeta} + \frac{\partial \tilde{F}_u}{\partial \xi} + \frac{\partial \tilde{F}_w}{\partial \zeta} \right)^{l-1}, \tag{25}$$

which can be solved through a tri-diagonal matrix algorithm (TDMA) for the pressure Fourier components p_k

$$k^2 p_k + \frac{\partial^2 p_k}{\partial \zeta^2} = R_k, \tag{26}$$

where R_k is the Fourier component for the right-hand side in Eq. 25. Approximation of a vertical derivative of p_k considers that a vertical profile of Fourier components for pressure can be approximated through the following function:

$$p_k(\zeta) = P_k(\zeta) \exp(-2|k|\zeta), \tag{27}$$

where the coefficients $P_k(\zeta)$ are a slowly changing function of ζ . To provide the continuity equation validity up to the surface $\zeta = 0$, boundary conditions for pressure are derived on the basis of the boundary conditions for a ‘vertical’ component of the surface covariant velocity \tilde{w}_0 and \tilde{w}_H :

$$\tilde{w}_0 = -u_0 z_\xi + w_0 x_\xi, \quad (28a)$$

$$\tilde{w}_H = 0, \quad (28b)$$

where u_0 and w_0 are the Cartesian components of the surface velocity. The calculated pressure is used for correction of the velocity field as presented in Eqs. 5a,b.

This method generalizes a standard approach for solution of the Navier–Stokes equations in curvilinear coordinates.

4 Mathematical Modelling of Waves

The approach based on non-stationary conformal mapping had been discussed long before it was applied for the numerical solution of wave equations. Such a transformation was first introduced by [Ovsyannikov \(1973\)](#), and later considered by [Kano and Nishida \(1979\)](#); [Fornberg \(1980\)](#) and [Tanveer \(1991, 1993\)](#). However, none of these works used conformal transformation for the simulation of the long-term multi-mode periodic wave dynamics. Such a 2-D model was completed in 1992, when a new approach to different problems came into use. The scheme for an arbitrary depth was described in detail by [Chalikov and Sheinin \(1996, 1998, hereafter ChSh\)](#). Later the method developed was used (with some minor modifications) by [Zakharov et al. \(2002, 2006\)](#) to demonstrate certain non-linear properties of steep waves.

Non-stationary conformal mapping for finite depths allows rewriting the principal equations of the potential flow with a free surface in a surface-following coordinate system. The Laplace equation retains its form, while the boundaries of the flow domain (i.e., a free surface, and a bottom) are coordinate surfaces in the new coordinate system. Accordingly, the velocity potential of the entire domain obtains a standard presentation based on the Fourier expansion for the velocity potential on a free surface. As a result, the full hydrodynamic system of equations is represented by two simple evolutionary equations that can be solved numerically in a straightforward way and used for theoretical study. The assumption of potentiality simplifies the approach so significantly that the numerical scheme does not require any finite-difference approximations, since the derivatives can be calculated precisely using the Fourier presentations, whilst non-linearities can be approximated on a dense grid with a well-estimated accuracy. For the restricted order of non-linearity this method is also precise and depends on the length of word assigned for the calculations. The model is a unique case in geophysical fluid dynamics, when a real process can be simulated with computer accuracy, provided that the surface steepness is not too high. The increase of the local steepness often results in the development of instability and even in the overturning of sharp crests. Formally, conformal mapping exists up to the moment when the overturning volume of water touches the surface. In such an imaginary evolution the number of Fourier modes required increases up to infinity. If some special measures are not taken, the calculations normally terminate much earlier due to the strong crest instability ([Longuet-Higgins and Tanaka 1997](#)) followed by a split of a falling volume into two phases. This phenomenon is obviously non-potential. Hence, as in many branches of the geophysical fluid dynamics, some special measures (which are sort of “humbug” from the point of view of the classical potential theory) must be undertaken

to prevent numerical instabilities, whilst considering physical consequences of the breaking events (e.g. conservation of volume, energy and momentum).

Recently, the ChSh model was used for the simulation of wave evolution at various initial conditions (Chalikov and Sheinin 2005). The numerical simulations of the initially monochromatic waves with a different steepness showed that the model was able to reproduce the onset of the breaking process when the surface becomes a multi-valued function of a horizontal coordinate. Then the model was used for the simulation of a non-breaking evolution of the wave fields with a greater number of modes for many periods of the dominant wave (Chalikov 2005, 2007). The statistical characteristics of the non-linear wave fields for waves of different steepness were studied, including spectra, kurtosis and skewness, dispersion relation and time scales, i.e. a typical ‘lifetime’ of waves. The ChSh model was also used for the numerical simulation of the small-amplitude and finite-amplitude Benjamin and Feir instability (Chalikov 2007). It is shown that the initially homogeneous train of the Stokes waves undergoes several phases of evolution. Finally the wave field turns into a random superposition of the nearly Stokes waves. If an initial steepness is large enough ($ak > 0.12$), some waves become high and asymmetric, and finally break. In the current work the initial conditions were assigned as a superposition of the Stokes waves with a pre-assigned initial spectrum and random phases.

Chalikov (2009) describes the results of more than 4,000 long-term (up to thousands of peak-wave periods) numerical simulations of the non-linear gravity surface waves. The simulations were performed for the study of extreme (“freak”) wave properties, as well as for the estimation of the statistics of such waves. A probability function for the steep waves was constructed. Such results can be used for the development of the operational freak wave forecast based on the third-generation wave prediction model (WAVEWATCH or WAM).

5 The Equations of the Wave Model

We consider the simulation of the coupled wind–wave dynamics on the basis of the WBL and ChSh models. The ChSh model shows that the potential wave equations can be represented in the coordinates (3) for $\zeta \leq 0$ and deep water as follows:

$$\Phi_{\xi\xi} + \Phi_{\zeta\zeta} = 0, \tag{29}$$

$$z_\tau = -x_\xi \xi_t - z_\xi \zeta_t, \tag{30}$$

$$\varphi_\tau = -\zeta_t \varphi_\xi - \frac{1}{2} J^{-1} (\varphi_\xi^2 - \Phi_\zeta^2) - z - p_0, \tag{31}$$

where (30) and (31) are written for the surface $\zeta = 0$ (so that $z = \eta$, as represented by expansion (1)), p_0 is the surface pressure, J is the Jacobian of the transformation:

$$J = x_\xi^2 + z_\xi^2 = x_\zeta^2 + z_\zeta^2, \tag{32}$$

and ξ_τ and ζ_τ are connected through the following relationship:

$$\zeta_t = - (J^{-1} \Phi_\zeta)_{\zeta=0}, \tag{33}$$

and $\varphi = \Phi (\zeta = 0)$.

Equations 6, 7, 8a,b, as well as equations for the WBL, are written in a non-dimensional form using the following scales: length L where $2\pi L$ is a dimensional period in the horizontal, time $L^{1/2}g^{-1/2}$ and the velocity potential $L^{3/2}g^{-1/2}$. The capillarity was not taken

into account in this investigation. The boundary condition assumes attenuation of the vertical velocity at depth:

$$\Phi_\zeta(\xi, \zeta \rightarrow -\infty, \tau) = 0. \quad (34)$$

The solution of the Laplace equation (29) with the boundary condition (34) is represented through the Fourier expansion, which reduces the system (29)–(31) to a 1-D problem:

$$\Phi = \sum_{-M \leq k \leq M} \phi_k(\tau) \exp(k\zeta) \vartheta_k(\xi), \quad (35)$$

where ϕ_k are the Fourier coefficients of the surface potential $\Phi(\xi, \zeta = 0, \tau)$. Equations 29–33 and 35 constitute a closed system of prognostic equations for the surface functions $z(\xi, \zeta = 0, \tau) = \eta(\xi, \tau)$ and the surface velocity potential $\Phi(\xi, \zeta = 0, \tau)$. For time integration, as well as for the WBL model, the fourth-order Runge–Kutta scheme was used, and selection of a suitable timestep was done empirically. Details of the numerical scheme can be found in Chalikov and Sheinin (2005).

However high the spectral resolution might be, for long-term simulations of strongly non-linear waves one must parameterize the energy flux into the severed part of the spectrum ($|k| > M$), otherwise, the spurious energy accumulation at large wavenumbers can corrupt the numerical solution. The simple dissipation terms were added to the right-hand sides of Eqs. 30 and 31 for achieving stability:

$$\frac{\partial \eta_k}{\partial \tau} = E_k - \mu_k \eta_k, \quad (36a)$$

$$\frac{\partial \varphi_k}{\partial \tau} = F_k - \mu_k \varphi_k \quad (36b)$$

where E_k and F_k are the Fourier components of the right-hand sides of the equations, and

$$\mu_k = \begin{cases} rM \left(\frac{|k| - k_d}{M - k_d} \right)^2 & \text{if } |k| > k_d \\ 0 & \text{if } |k| \leq k_d \end{cases}, \quad (37)$$

where $k_d = M/2$ and $r = 0.25$ were chosen for all the runs discussed below. Sensitivity of the results for reasonable variations of k_d and r was low. Dissipation effectively absorbs energy if wavenumbers are close to the truncation number M , longer waves being virtually intact. The modes with wavenumbers $|k| \leq k_d$ are not affected at all. Note that an increase of the truncation number M shifts the dissipation area to higher wavenumbers (and, with $M \rightarrow \infty$, the energy sink tends to zero due to dissipation), so the dissipation scheme described above retains an approximation of the original (non-dissipative) system.

The problem of the numerical scheme validation for the wave model was discussed in ChSh, Chalikov and Sheinin (2005) and Chalikov (2005). The scheme was found to be very precise: a normal accuracy of solution for a sufficiently high resolution was around 10^{-10} . This is no surprise, since the equations written in conformal coordinates become the one-dimensional evolutionary equations that can be accurately solved by means of the Fourier transform method using no local approximations. A high accuracy of the solution and preservation of the integral invariants is crucial for a numerical wave simulation, as the ratio of time scale for waves and that for the energy input and dissipation is on the order of 10^{-4} , so the wave motion is highly conservative, while at time scales of the order of a wave period it is actually adiabatic.

There is a unique possibility for validation of the numerical model by comparison of the solution of full equations with the exact solution. Some algorithms for generation of all the types of the stationary waves, as well as validation of the non-stationary model, were described in ChSh. Propagation of very steep Stokes waves ($ak = 0.42$) was simulated by Chalikov (2005) over 2,686,500 timesteps (932 periods). The total energy reduction for the number of modes $M = 1,000$ occurred only within $3 \times 10^{-8}\%$. Similar calculations for $ak = 0.42$ carried out by Dold (1992) rapidly collapsed due to the numerical instability. The exact phase velocity of the Stokes waves ($ak = 0.42$), obtained for the stationary solution is 1.089578. The direct calculations of the phase velocity for the simulated Stokes wave gave the value of 1.089579 ± 10^{-6} . The same procedures were performed for the stationary analytical solution for the capillary waves (Crapp 1957) as well as for the gravity-capillary waves of varying capillarity (see ChSh). Such experiments proved the highest accuracy of the scheme based on the conformal transformation. Note that the validation of the model based on simulation of the exact Stokes waves assigned in the initial conditions is full and not trivial.

The adiabatic version of the equations of wave theory (not necessarily potential) has a very important property of *self-similarity*: a non-dimensional form of the equations (outside of a capillary range) does not include a non-dimensional parameter. It means that due to the simple scale transformation the numerical results can be used for analysis of the gravity waves of any scales for the same non-dimensional initial conditions. The self-similarity of the equation simplifies the study of wave dynamics, since the solution depends on the initial conditions only, and each single run based on the non-dimensional equations corresponds to an infinite number of real cases.

Over the last few years great attention has been given to the effect of breaking (Babanin 2009). In our opinion, the role of breaking for the air boundary layer is overestimated. A non-linear dependence of the pressure extremes on the wave steepness plays a more important role, while the influence of breaking on the WBL is just a consequence of such a dependence. Breaking is the main mechanism of wave dissipation. A scheme based on conformal mapping allows approaching very closely to the breaking point. In fact, the integration always terminates in this way; still, due to high accuracy of the scheme, such modelling of the instability represents an example of the unique case in fluid dynamics when a numerical and physical instability follow each other in close succession. We use two ways of interpreting the breaking process. When breaking is a subject of investigation per se, it is simulated directly up to the point of the instability. The last non-realistic stage of breaking can be easily detected through the energy conservation control. The final stage of breaking is evidently non-potential. Such a direct method is inapplicable if the wave model is used for a long-term coupled simulation when studying the WBL structure, the wave drag and the energy exchange.

In long-term coupled simulations the termination is not desirable. This is why an algorithm of the breaking parameterization based on smoothing of the interface was developed. The algorithm (the basic concept of the algorithm is very close to that used for parameterization of free convection in atmospheric models) is designed to prevent the breaking instability by highly selective high-frequency smoothing of the interface profile. Many schemes to parameterize such a phenomenon were tested, the most efficient being based on the simple diffusion-type algorithm:

$$\eta_\tau = E_\eta + J^{-1} \frac{\partial}{\partial \xi} B \frac{\partial \eta}{\partial \xi}, \quad (38a)$$

$$\varphi_\tau = F_\varphi + J^{-1} \frac{\partial}{\partial \xi} B \frac{\partial \varphi}{\partial \xi}, \quad (38b)$$

where E and F_Φ are the right-hand sides of Eqs. 32 and 33, whilst the coefficient of diffusion B depends on the second derivative of the interface:

$$B = \begin{cases} C_b \left(\Delta \xi \frac{\partial^2 z}{\partial \xi^2} \right)^2 & \frac{\partial^2 z}{\partial \xi^2} > s \\ 0 & \frac{\partial^2 z}{\partial \xi^2} \leq s \end{cases}, \quad (39)$$

where the coefficient C_b is of the order of 0.1, and the critical value of the second derivative s is of the order of 300. The algorithm of the ‘tail dissipation’ (38, 39) does not change the volume but reduces the energy and momentum of waves. It is assumed that some portion of the energy (and momentum) loss is transferred to the horizontal flow, while another portion is transferred to turbulence (such transformations can be considered separately, see Chalikov and Belevich 1993). Evidently the potential wave model cannot assimilate anything but a normal stress component.

Parameterization of the rotational breaking in the potential model allows us to effectively prevent development of the breaking instability. Such a scheme does not influence the solution in the absence of breaking. We do not consider this algorithm as the final solution of the problem, since it cannot prevent collapse in the cases of very high initial steepness or energy. However, for the normal steepness of sea waves, and for the cases of a relatively slow growth of the local energy, it works well.

6 Coupling of Wave Models with the Model of the Wave Boundary Layer and Description of Numerical Experiments

The coupled model consists of the two main components: the wave model and the WBL model. Both of the models must be integrated simultaneously. However, there is a small parameter in the coupled problem, i.e., the ratio of density for air and water $\rho_a/\rho_w \approx 10^{-3}$. This is why coupled modelling can be carried out as a separate time stepping with exchange of matching information at each timestep. The WBL model calculates boundary conditions for the wave model: the surface pressure p_0 and the normal turbulent stress providing exchange by momentum and energy between air and water. The wave model calculates a shape of the interface $\eta(\xi)$, a rate of the ‘vertical’ displacement η_τ , required for the calculation of the metric coefficients for the WBL model and the surface velocity components u_0 and w_0 , as a boundary condition for the Poisson equation for pressure, and for the calculation of the tangential stress τ_t on the interface. Along with the surface pressure p_0 , the tangential stress τ_t is responsible for formation of a constant-stress layer in the WBL. τ_t cannot be assimilated in the wave model due to potentiality.

The specific problem of coupled modelling is that the initial data are normally given in Cartesian coordinates, but they need to be converted into (ξ, ζ) coordinates. For this purpose and for post-processing of the results a precise interpolating algorithm based on the periodic high-order spline functions was developed.

In this study the method of approximation of initial conditions by superposition of the Stokes waves developed in Chalikov (2005) was used. Briefly, the method is based on the use of ‘upper conformal coordinates’ (Eq. 3) where $\zeta > 0$ (ξ_u, ζ_u). It was shown that the superposition of the linear waves assigned in this coordinate system, after interpolation to Cartesian coordinates, turns into the superposition of the Stokes waves with high accuracy. Note that the full equations at any reasonable initial conditions (after a certain accommodation period) reproduce this effect too, since harmonic waves tend to turn into Stokes-like

waves. Herein an initial generation of Stokes waves was used to accelerate transition to the statistically homogeneous regime.

In this study we applied the above method for the numerical simulation of the surface waves for investigation of evolution of a wave field assigned by the one-dimensional version of the JONSWAP spectrum S_f for finite fetch as a function of frequency ω ,

$$S_f(\omega) = \frac{\alpha g^2}{\omega^5} \exp\left(-\beta_1 \left(\frac{\omega_p}{\omega}\right)^4\right) \gamma^r, \tag{40}$$

where $\beta_1 = 1, 25$, $\gamma = 3.3$, ω_p is a parameter whose value is close to the frequency of the spectral peak S_p . Other parameters can be expressed through ω_p :

$$r = \exp\left(-\frac{(\omega - \omega_p)^2}{2\sigma^2\omega_p^2}\right), \tag{41a}$$

$$\alpha = 0.0099\Omega^{0.66}, \tag{41b}$$

$$\sigma = \begin{cases} 0.07 & \omega \leq \omega_p \\ 0.09 & \omega > \omega_p \end{cases}, \tag{41c}$$

where

$$\Omega_p = \frac{\omega_p U_{10}}{g} = \frac{U_{10}}{c_p}, \tag{42}$$

is the non-dimensional frequency in the spectral peak and c_p is the peak phase velocity.

It is well-known that approximation (40) overestimates the spectrum at low values of the non-dimensional frequencies $\Omega \leq 1.3$ (high fetches). To maintain the right asymptotic behaviour, the approximation (40) was combined with the Pierson–Moskowitz (PM) spectrum for the fully developed waves

$$S_\infty(\omega) = \frac{\alpha g^2}{\omega^5} \exp\left(-\beta_2 \left(\frac{\omega_0}{\omega}\right)^4\right) \tag{43}$$

through the following relation:

$$S = S_\infty W + S_f(1 - W), \tag{44}$$

where W is a weight that is convenient to represent as a function of Ω . It is easy to show that $\Omega_\infty = 0.855$ for the PM spectrum. Since transition from the spectrum S_∞ to S_f happens in a small interval of Ω , the function W quickly decays with growth of $\Omega_p - \Omega_\infty$. The function $W(\Omega)$ was approximated by

$$W = \exp(-15(\Omega_p - \Omega_\infty)). \tag{45}$$

In the initial JONSWAP approximation the enhancement parameter for the spectrum γ was accepted as constant: $\gamma = 3.3$. Later some investigators came to the conclusion that the above parameter can be a function of the fetch or peak frequency ω_p . According to Babanin and Soloviev (1998), γ increases with Ω_p as $\gamma = 1.224 \Omega_p$.

Merging (44) is done in a very narrow interval [0.855 to 1]. The number of cases falling in this interval is so small that it does not influence the statistics. Approximations (40)–(43) were rewritten in terms of wavenumbers using the linear dispersion relation that is valid at least up to $3\Omega_p$ (Chalikov 2005). The non-dimensional wavenumber k_p at the spectral peak is a parameter of initial conditions. To describe the low wavenumber slope of the spectrum, k_p should exceed 1, while for a good approximation of the entire spectrum, as well as for

spectrum spreading due to non-linearity, k_p should be considerably smaller, as compared with the total number of modes M . Actually, k_p is the parameter of the accuracy of approximation.

The best way of modelling of the WBL might be based on a very high spectral resolution for reproduction of large and small waves including capillary waves. One can imagine that for such calculations the number of modes should not be less than 10,000. A high horizontal resolution suggests a high vertical resolution; consequently, the number of levels in the WBL should be about 100 and the total number of knots should be equal to 400,000. Such calculations can be performed only for a few cases. Hence, a moderate resolution for obtaining rich statistical data on the WBL structure was assigned (see below for the description of the numerical experiments). If the wave spectrum is not resolved up to a high wavenumber, the problem of parameterization of the subgrid waves arises. By analogy with the solid rough surface, we assume that the local roughness parameter z_l is proportional to root-mean-square (rms) height h_r of the ‘roughness elements’, i.e. to the typical height of all subgrid waves:

$$z_l = 0.03 \left(\alpha \int_M^{k_r} k^{-3} dk \right)^{1/2} = 0.0027k_r^{-1} \tag{46}$$

Finally, the local drag coefficient in Eq. 15 can be calculated as follows:

$$C_l = \kappa^2 \left(\ln \frac{z_1}{z_l} \right)^{-2}, \tag{47}$$

The initial conditions for the Fourier coefficients of the free surface $\eta(x)$ were assigned in the following form:

$$|h_k| = (2S(k)\Delta k)^{1/2}, \tag{48a}$$

$$\eta_k = |h_k| \cos(\varphi_k), \tag{48b}$$

$$\eta_k = |h_{-k}| \sin(\varphi_k), \tag{48c}$$

where $k = 1, 2, 3, \dots, M$, $|h_k|$ is the amplitude of the k th mode, M_i is the number of modes assigned for initial conditions, η_k, η_{-k} are the Fourier coefficients, and φ_k are the random (over k and over different runs) phases distributed uniformly over the interval (0 to 2π). The Fourier coefficients f_k for the surface potential $f(x)$ were assigned through:

$$f_k = -|k|^{-1/2} a_{-k}, \tag{49}$$

for $k = -M_i, M_i$. Following the inverse Fourier transform, functions $\eta(x)$ and $f(x)$ were transferred from the ‘upper coordinates’ to the ‘lower coordinates’ by means of periodic spline interpolation providing accuracy of the order of 10^{-10} for very steep waves, and 10^{-30} for the medium-amplitude waves. Post-processing was done for the data transferred to the Cartesian coordinate by the inverse algorithm. For the spectrum assigned in the form of (40)–(44) for the integral rms steepness less than 0.09 the breaking instability never occurs. For the rms steepness of the order of 0.15 the breaking instability occurs immediately within one peak wave period.

7 Evolution of Waves

Figure 1 clearly illustrates the essence of the problem being solved. The figure represents an instantaneous image of interacting flows for the case of the initial wave field assigned as a

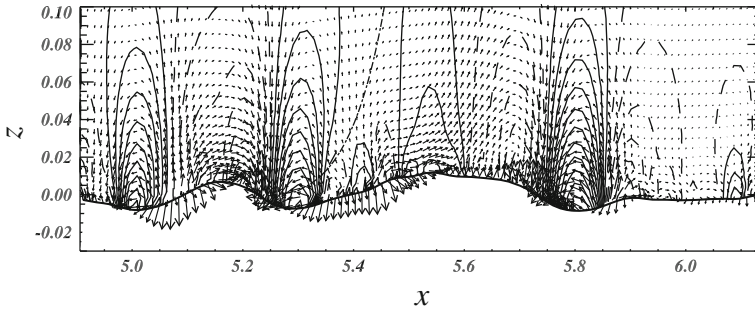


Fig. 1 An example of 2-D flow structure above waves. The contours represent pressure distribution (*solid lines* correspond to positive values, *dashed lines* to negative values); *arrows* are vectors of wave-produced velocity. A small fragment of the reproduced field is drawn: the total height of domain is about 0.7; length equals 2π

superposition of 1,000 linear (in the upper coordinate system) wave modes corresponding to the JONSWAP spectrum for the non-dimensional peak frequency $\Omega_p = U_{10}/c_p = 2$. The number of knots over the ‘horizontal’ coordinate ξ equals 4,000; over the ‘vertical coordinate’ ζ the number of levels equals 70; the stretching parameter γ equals 1.07. In fact, the coupled model simulates a periodic process in the circular wind–wave tunnel, although with neither wave reflection from the walls nor centrifugal acceleration. The periodic domain includes 16 peak waves. It is impossible to show the entire domain with length $L = 2\pi$ and height $H_a = 0.7$, so Fig. 1 shows only a small fragment with the non-dimensional height equal to 0.1 and the non-dimensional length equal to 1.2. The solid periodic curve corresponds to water elevation distorted by dispersing waves. The contours within the air domain represent the distribution of pressure (solid lines correspond to positive anomalies, while dashed lines show negative anomalies). The smooth curve in the middle of the picture shows the averaged wind profile. The wind and waves are directed from left to right. The non-dimensional wind speed at the top edge of the picture equals 0.5, while the non-dimensional peak phase velocity equals 0.25. The waves demonstrate a tendency for peak sharpening and trough smoothing. The vectors in Fig. 1 describe a wave-produced velocity field, and the largest distortions of the pressure and velocity fields occur behind the wave crests of high waves. In general, negative anomalies of pressure and high gradients of wave-produced velocities are concentrated in the narrow intervals with high negative steepness of wave surface. Such intervals appear more frequently than those with high positive steepness, e.g. a wave has a tendency for inclining forward, while a flux of energy depends non-linearly on the local steepness. The spectral representation of such pressure becomes less meaningful, since the high wavenumber Fourier modes do not correspond to real waves; they rather provide the approximation of the impulse-like negative anomalies of the pressure. The positive anomalies of the pressure are distributed more or less smoothly over the areas of either positive or small steepness. On the whole, such a pressure field generates a positive flux of momentum from wind to wave.

The main advantage of the mathematical ‘wind–wave channel’ is the possibility of generation of the full set of all kinematic and dynamic fields. It is easy to install a ‘sensor’ for the registration and calculations of any statistical and spectral characteristics including high-order moments. The total E_t , kinetic E_k and potential E_p wave energies are defined as

$$E_p = (2\pi)^{-1} \int_0^{2\pi} z^2 x_\xi^2 d\xi, \tag{50a}$$

$$E_p = (2\pi)^{-1} \int_0^{2\pi} \varphi \varphi_\tau d\xi, \quad (50b)$$

$$E_t = E_p + E_k. \quad (50c)$$

The rate of energy exchange between air and waves can be calculated as follows:

$$F_t = \overline{p\eta_\tau} + \overline{\tau'_0 u'_0 x_\xi}, \quad (51)$$

where the first term describes the work of the surface pressure, while the second term describes the work of the tangential stress. In general, the flux of energy is directed from wind to waves, although in some cases, when the wave spectrum includes a swell whose phase velocity is higher than the wind speed, the energy is directed from waves to wind (i.e., waves accelerate the flow). Such waves are always present in the wind–wave spectrum, though the effect of the inverse flux of energy in the low-frequency spectral range is insignificant for the WBL. However, this process can contribute to the dissipation of the swell.

The integral rate of kinetic D_k and potential D_p energy dissipation is calculated as

$$D_k = \overline{\eta(\eta_\tau)_d}, \quad (52a)$$

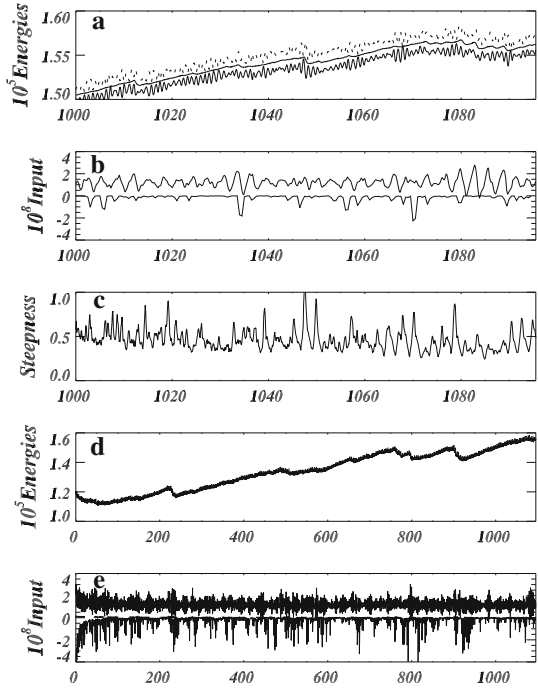
$$D_p = \overline{\varphi(\varphi_\tau)_d}, \quad (52b)$$

$$D = D_k + D_d, \quad (52c)$$

where $(\eta_\tau)_d$ and $(\varphi_\tau)_d$ are the sum of the dissipation terms. Equations 52a–c includes the ‘tail dissipation’ (36a,b) describing the flux of energy into the subgrid wavenumbers, and the breaking dissipation described by Eqs. 38a,b. Note that the wave profiles often do not contain any intervals affected by breaking; however, the dissipation due to breaking (when it does occur) is normally greater by orders of magnitude comparing to the ‘tail dissipation’.

The evolution of the wave energy, input and dissipation of energy for the initial conditions assigned by the JONSWAP spectrum at $\Omega_p = 2$, is shown in Fig. 2. In this run the wave field was initially represented by 100 wave modes with $k_p = 16$ and $M = 1,000$. The wave energy increases due to the action of wind. The evolution of the potential energy E_p (the thin curve), kinetic energy E_k (the dotted curve) and total energy $E_t = 0.5(E_p + E_k)$ (the thick curve, see Eq. 50c) over the last 30 peak wave periods, is represented in panel a. The potential and kinetic energies averaged over the period $(0, 2\pi)$ rapidly fluctuate, but these fluctuations are not pronounced for the averaged total energy E_t . The energy input to waves (panel b, the upper curve) also fluctuates due to the variable wave steepness represented in frame c by the highest absolute value of the steepness in every instantaneous wave profile. In most cases the negative steepness is stronger than the positive one, since waves are asymmetric (i.e., inclined forward). The steepness in panel c is taken with an opposite sign. As seen, enhancement of the energy input and energy dissipation develops with an increase of steepness. Such fluctuations cannot be explained on the basis of the linear theory. Frame d shows the same evolution over the total interval of integration (about 370 periods of the peak wave periods); in this frame the curves for E_p , E_k and E_t merge into one thick curve. The bottom frame e shows the evolution of the total input of energy (the upper fluctuating curve) and its dissipation (the bottom curve). The dashed straight line close to the zero line corresponds to the input of energy to waves through the tangential stress, which is much smaller than the input provided by the pressure field. The input of energy is strongly intermittent. Such intermittency occurs since the input depends rather on the surface geometry in physical space than on the spectrum (which fluctuates slowly in the energy-containing part).

Fig. 2 **a** Evolution of potential E_p (thin curve), kinetic E_k (dotted curve) and total $E_t = 0.5(E_p + E_k)$ (thick curve) energies (Eqs. 50a–c) over the last 30 peak wave periods; **b** evolution of input (upper curve, Eq. 51) and dissipation D (lower curve, Eqs. 5a–c) of energy for the same period; **c** evolution of the highest steepness (with an opposite sign) in a wave profile; **d** evolution of energy over the total interval of integration (about 370 periods of peak wave periods). In this frame the curves for E_p , E_k and E_t merge; **e** evolution of the total input (upper curve) and dissipation (lower curve) for the same period



Note that, according to linear theory, the input energy should be very stable and can change due to variations of spectrum.

8 The 1-D Structure of the 2-D WBL

The main difference between the WBL and the boundary layer above the flat surface is the presence of a moving curvilinear interface between water and air. In linear theories such finite amplitude fluctuations of the interface are actually ignored, however, in the mathematical simulations such an approach is unacceptable. Numerical modelling of the boundary layer and waves is impossible to carry out in the Cartesian coordinate system, which is the main reason for the introduction of surface-following coordinates. The dynamic equations in the curvilinear coordinates are more complicated compared with the standard form equations. Fortunately the 2-D case allows introduction of conformal coordinates. The equations written in such coordinates are not simple, though they are much simpler compared to equations in general curvilinear coordinates. Moreover, the equations written in conformal coordinates can be easily interpreted. The main advantage of the surface following coordinates (2) is that water and air domains are separated by the coordinate $\zeta = 0$. The natural boundary condition above the flat surface is $w = 0$ at $z = 0$, while in conformal coordinates the ‘vertical’ contravariant velocity W acquires the role of the vertical velocity w . Since a kinematic condition on the surface is $W = 0$, the exchange by finite volumes through the interface is absent.

Let us average the equation for the horizontal momentum (5a) over the coordinate $\zeta = \text{constant}$

$$\frac{\partial \langle Ju \rangle}{\partial t} = \frac{\partial}{\partial z} \left(\underbrace{-\langle uW \rangle}_{(I)} + \underbrace{\langle pz\xi \rangle}_{(II)} + \underbrace{\langle -z\xi \overline{u'u'} + x\xi \overline{u'w'} \rangle}_{(III)} + \underbrace{\langle \overline{u'w'} \rangle}_{(IV)} \right) \quad (53)$$

which is the equation of the horizontal momentum balance. The brackets $\langle \rangle$ denotes averaging along ξ over the period $[0, 2\pi]$. Since $\langle \zeta \rangle = z$ and $\langle \partial/\partial \zeta \rangle = \partial/\partial z$, Eq. 54 can be considered as written in the Cartesian coordinate system.

The rate of momentum change depends on the vertical divergence of the vertical momentum flux provided by the wave-produced velocities (I), pressure (II), fluctuations of stresses (III) and the averaged turbulent flux (IV). Equation 53 is similar to the standard equation of momentum balance above the flat surface:

$$\frac{\partial u}{\partial t} = \frac{\partial \langle u'w' \rangle}{\partial z}, \quad (54)$$

although the Eq. 53 takes into account additional mechanisms of the vertical momentum transport. Note that, contrary to Eq. 54, the averaging in Eq. 53 is performed along the curvilinear paths. Such averaging is suitable in the presence of the curvilinear surface, since the surface kinematic condition $W = 0$ at $\zeta = 0$. Equation 54 makes no sense for the case with a curvilinear boundary, since Eq. 54 can be derived by averaging beyond the highest elevation in ensemble only. Through the interface momentum is transferred by the pressure field and tangential stresses. Since the wave model is potential, it cannot assimilate the tangential stress; therefore, waves obtain energy mostly through the surface pressure field.

For investigation of the vertical structure of the WBL the results of the long run described in the previous section were used. The instantaneous wave-produced fluctuations of pressure have an irregular structure, however, being averaged over time, they exhibit distinct regularities. The averaged vertical profiles of the spectral component of the pressure P_k are shown in the upper panel of Fig. 3, where the pressure spectrum decays exponentially with height. After normalization of each profile by the surface value of pressure, and introduction of the vertical coordinate kz , the profiles of P_k become more or less universal and can be approximated through the following relation:

$$P_k = P_{0k} \exp(-A_p kz), \quad (55)$$

where P_{0k} is the surface value of P_k , A_p is the decrement falling within the range $0.6 < A_p < 0.7$. Hence, the wave-produced pressure fluctuations in the turbulent flow attenuate at a slower rate as compared with the pressure fluctuations in potential waves. The spectrum of the kinetic energy of the wave-produced velocity fluctuations demonstrates a similar behaviour, the decrement A_e varying within the range $0.6 < A_e < 1.0$.

An example of the surface pressure spectrum is shown in Fig. 4 (curve 2), where curves 1 and 3 show the elevation spectrum and the spectrum of the near-surface kinetic energy respectively. The straight line 5 corresponds to the dependence $S_k \sim k^{-3}$. As seen, the high wavenumber part of the spectrum maintains its shape with a good accuracy. The spectrum of the near-surface kinetic energy attenuates slower with increase of wavenumber, as compared with the wave spectrum. It is interesting to note that the maximum of the surface pressure spectrum is shifted from the maximum of the wave spectrum to higher wavenumbers. The maximum of the pressure spectrum is located in the vicinity of the maximum of spectral steepness S_k (curve 4) defined by the following expression:

$$S_k = k\sqrt{S\Delta k}, \quad (56)$$

(k is the wavenumber, S represents values of the wave spectrum, $\Delta k = 1$). Hence, anomalies of the surface pressure depend rather on steepness than on the wave amplitudes.

Fig. 3 Spectral structure of the pressure field. *Upper panel*—vertical profiles of Fourier amplitudes for pressure P_k . *Bottom panel*—vertical profiles of pressure Fourier amplitudes, normalized by their surface value P_{0k} as a function of non-dimensional height kz

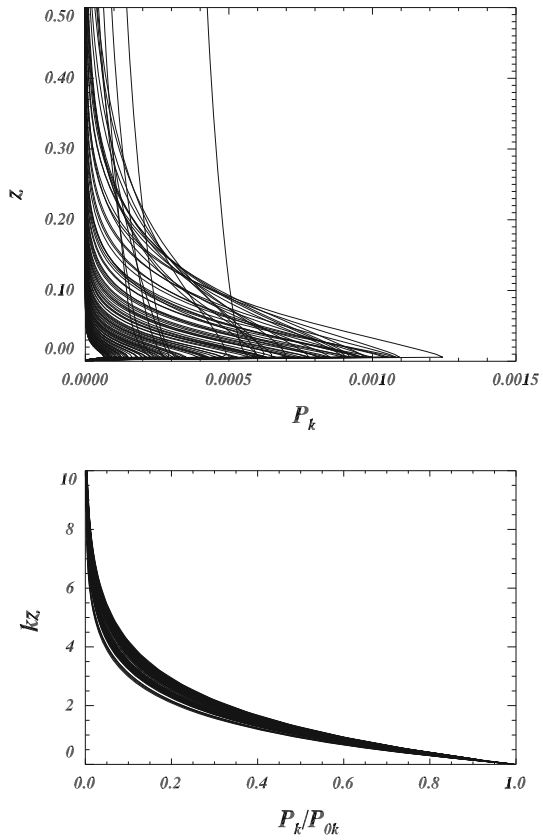
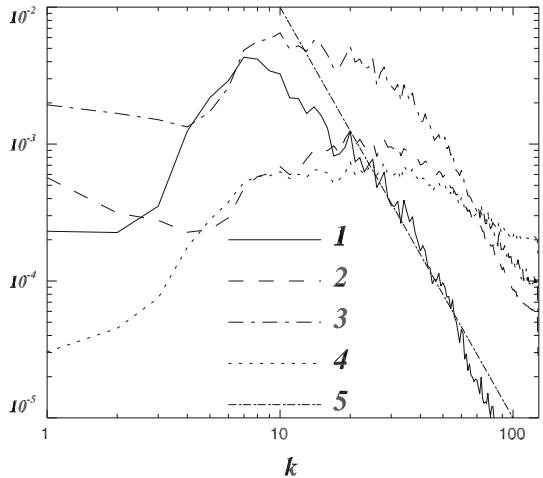


Fig. 4 Typical spectra of: surface elevation—*curve 1*, surface pressure—*2*, surface kinetic energy—*3*, spectral steepness—*4* (Eq. 56). *Straight line 5* corresponds dependence $S_k \sim k^{-3}$



Different components of the vertical momentum flux (Eq. 53) normalized by the outer stress τ as a function of z/L_p ($L_p = 2\pi/k_p$), are given in Fig. 5; the aggregated grey lines are instantaneous profiles, while the solid lines are averaged profiles. As seen, all of the

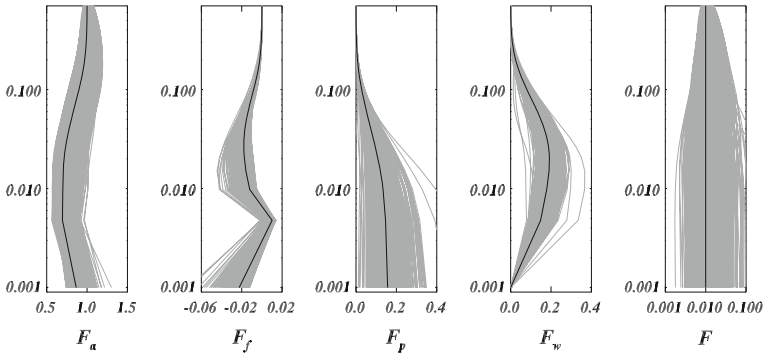


Fig. 5 Different components of the vertical momentum flux as a function of z/L_p (vertical axis) normalized by the outer stress τ (see Eq. 53). Aggregated grey lines are instantaneous profiles; solid lines are averaged profiles: F_a —an averaged turbulent momentum flux (0th mode, term IV in Eq. 53); F_f —momentum flux provided by wave fluctuations of turbulent stresses (term III); F_p —momentum flux provided by the pressure field (term II); F_w —momentum flux provided by the velocity field (term I); F —the total momentum flux

components of the wave-produced momentum flux (WPMF) are concentrated in the vicinity of the surface in the layer whose thickness is of the order of $0.2L_p$. The averaged turbulent momentum flux F_a (term IV in Eq. 53) transfers momentum to the averaged flow in the water (drift currents). F_a reaches the minimum value 0.7τ at height $z = 0.01L_p$ and equals 0.9τ on the surface. Hence, at given spectral resolution only 10% of the total stress is transferred to the waves. The flux of momentum transferred by fluctuating turbulent stresses F_f (term III in Eq. 53) is quite insignificant, which means that a correlation between the tangential surface stress and a tangential component of the orbital velocity is weak. Pressure transfers the main part of the momentum to waves, F_p (term II in Eq. 53). In the given case this flux increases monotonically upon approaching the surface where it reaches the value of 0.15τ . However, it should be emphasized that the surface value of F_p depends on the spectral resolution (see Sect. 10). With an increase of the ‘cut frequency’ this value grows, almost reaching the value of the total stress τ . The flux of momentum transferred by the velocity field F_u (term I in Eq. 53) reaches its maximum at a height $z/L_p \approx 0.1$, and then decreases upon approaching the surface. F_u becomes strictly equal to zero at the surface due to the surface kinematic condition.

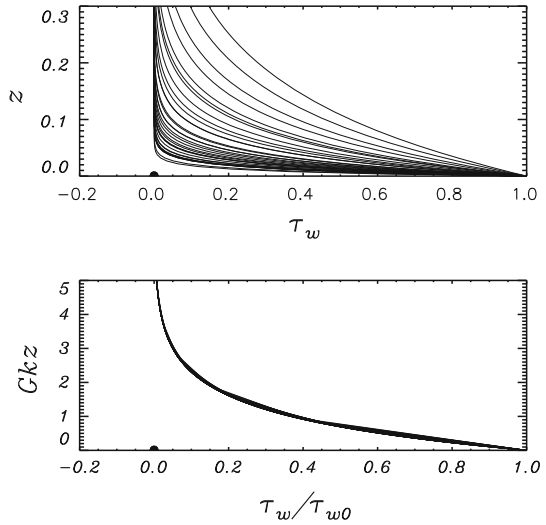
Let us define the k th spectral component of the wave-produced momentum flux τ_w^k as the Fourier component of the total momentum flux to waves, i.e. the sum of the I, II and III terms in Eq. 53. The averaged profiles of the spectral components of the WPMF calculated over the entire run are shown as a function of z in Fig. 6. As seen, the shapes of the profiles considerably depend on the wavenumber. These data can be regularized by normalization with the surface values of τ_w^k ; and by introduction of the non-dimensional wave height kz , in the same way as was done with the data shown in Fig. 3. After such a transformation the profiles of τ_w^k appear as the profiles in the bottom panel of Fig. 3. However, such a regularization can be much more precise if the following dependence is introduced:

$$\tau_w^k = \tau_{w0}^k \exp(Gkz), \tag{57}$$

where G is the weak function of $\tilde{\omega} = \Omega/\Omega_p$,

$$G = 0.985 + 0.4(\tilde{\omega})^{0.81}, \tag{58}$$

Fig. 6 The upper panel: vertical profiles of the total wave produced momentum flux (WPMF) F_{twp} as a function of z ; lower panel—the same profiles but normalized by surface values as a function of Gkz (Eq. 59)



noting that $\bar{\omega}$ is also equal to the ratio of the dimensional frequencies ω and ω_p .

The spectral components of the profiles of τ_w/τ_{w0} are presented in the lower panel in Fig. 6 as a function of Gkz . As can be seen, Eq. 57 provides a satisfactory parameterization of the vertical profile of the WPMF spectral components. Note that the results discussed below do not change significantly, if the function $G(\bar{\omega})$ is replaced with a constant.

9 Evaluation of the β Function

According to linear theory, the Fourier components of the surface pressure p_0 are related to the Fourier components of surface elevation through

$$p_k + ip_{-k} = (\beta_k + i\beta_{-k})(h_k + ih_{-k}), \tag{59}$$

where β_k and β_{-k} are real and imaginary parts of the β function (i.e. the Fourier coefficients at cosine and sine respectively). It is a traditional suggestion that both coefficients are a function of the non-dimensional frequency $\Omega = \omega_k U$ (where U is the non-dimensional wind speed). It would be quite reasonable to suggest that the reference level for the wind speed can be different for different frequencies; hence, the non-dimensional frequency Ω can be defined in the following way:

$$\Omega = \omega_k U (\lambda_k/2) = U (\lambda_k/2) / c_k, \tag{60}$$

where $\omega_k = |k|^{1/2}$ is the non-dimensional frequency, c_k is the phase velocity of the k th mode, and U is the non-dimensional wind speed at height $\zeta = \lambda_k/2$, where $\lambda_k = 2\pi/k$ is the length of the k th mode.

One of the main tasks of the present investigation is the evaluation of the β function over a wide range of the non-dimensional frequency Ω . For this purpose 47 long-term (up to several hundred peak wave periods) numerical runs with various wind speeds and spectral resolutions were performed using the coupled wind–wave model (see Table 1).

The wind speed at the upper level of the domain was assigned through different values of the stress $\tau = v_* |v_*|$ directed along and against the overall movement of waves. The main characteristics of the runs are indicated in Table 1. A stretching coefficient for the vertical grid γ was taken as 1.07, while some experiments were repeated for $\gamma = 1.05$ and even for $\gamma = 1.01$. The peak of the spectrum was usually placed at the wavenumber $k_p = 4$, although runs 29 and 30 were carried out at $k_p = 8$, and runs 36–44 at $k_p = 16$. The total number of modes M was normally equal to 100, while several runs intended for validation of the results were repeated for $M = 200$, $M = 1,000$ and $M = 2,000$.

It should be noted that, though the algorithm of the breaking parameterization (38), (39) was activated, some runs lapsed due to the breaking instability that occurs following the approach of a downwind slope to the vertical. To resume another run in automatic mode, a criterion for the run termination was defined as the first appearance of a non-single value of the surface η in the Cartesian coordinates:

$$x(i + 1) < x(i) \quad (61)$$

for $i = 1, 2, 3, \dots, N - 1$. It is possible to continue integration for the non-single-value surface (see Chalikov and Sheinin 2005), but the details of the process are not the subject of the current study. It is important to note that, upon reaching the criterion (61), stability is never restored: the volume of fluid crossing the vertical $x(i)$ quickly increases. The overturning always starts at the crest of the steepest wave. At the initial stage of such an evolution the conservation of invariants remains good; still, later, a sharp increase in energy occurs, and further integration becomes pointless. Usually instability develops throughout one Runge–Kutta timestep; the main reason for such numerical instability is growth of the right-hand sides of Eqs. 30 and 31. Application of the dynamic timestepping (similar to that used by Zakharov et al. 2002) can prolong run ‘agony’, though for quite a short period of time. The numerical instability exhibiting itself in breaking has a physical origin: in reality a falling water volume becomes rotational and splits into small patterns (i.e., a white capping phenomenon).

Strengthening of stability can be achieved by an increase of the C_b value and by a decrease of the ν value in Eq. 39; in this case sharp wave crests become smoother, which weakens the dynamic interaction between wind and waves. It was the reason for choosing relatively soft smoothing. Any criterion for identification of breaking, introduced for highly idealized conditions (Banner and Pierson 2007), turned out to be inapplicable. In reality the local breaking in a multi-mode wave field occurs for some inexplicable reason. The duration of a run (T_p in Table 1, expressed in periods of a peak wave) is found to be dependent even on a set of initial phases for modes.

Each run performed for different values of Ω_p provided data required for the calculation of $\beta(\Omega)$ within the interval $[\Omega_{\min}, \Omega_{\max}]$ (see Table 1). As seen, the data cover the interval $-50 < \Omega < 50$.

The total number of 1-D records of the wave surface (each of them containing from 400 to 8,000 points) was equal to 27,802. After the Fourier transform of each of such records, the first 50 complex Fourier coefficients for p_0 and η were used for the calculations of the β function. The total number of points falling within the interval $-50 < \Omega < 50$ was equal to 1,390,100. For estimation of β values the above interval was separated into 100 bins with the width of $\delta\Omega = 0.1$, and the number of points falling within each interval was roughly the same, i.e. around 14,000.

Table 1 Parameters of runs: v_* —friction velocity; $\Omega_p = u(\lambda_k/2)/c_p$; (Ω_{\min} , Ω_{\max})—range of Ω_k covered by run; T_p —length of run (expressed in peak wave periods); γ —stretching coefficient for vertical grid; k_p —peak wavenumber

No.	v_*	Ω_p	Ω_{\min}	Ω_{\max}	T_p	γ	k_p
1	-0.50	-28.75	-48.97	-10.65	57.3	1.07	16
2	-0.40	-24.78	-43.64	-8.97	89.1	1.07	16
3	-0.30	-20.31	-37.04	-7.16	12.7	1.07	16
4	-0.30	-20.31	-37.04	-7.16	19.1	1.07	16
5	-0.20	-8.97	-28.75	-5.18	127.3	1.07	4
6	-0.15	-7.16	-23.72	-4.10	127.3	1.07	4
7	-0.10	-5.18	-17.84	-2.94	222.8	1.07	4
8	-0.10	-5.18	-17.84	-1.64	79.6	1.07	4
9	-0.05	-2.94	-10.65	-1.64	95.5	1.07	4
10	-0.0125	-0.91	-3.53	-0.50	95.5	1.07	4
11	-0.00625	-0.50	-1.98	-0.27	12.7	1.07	4
12	-0.00313	-0.27	-1.10	-0.15	87.5	1.07	4
13	0.00313	0.27	0.15	1.10	76.4	1.07	4
14	0.00625	0.50	0.27	1.98	103.5	1.07	4
15	0.0125	0.91	0.50	3.53	350.1	1.07	4
16	0.025	1.64	0.91	6.19	159.2	1.07	4
17	0.05	2.94	1.64	10.65	127.3	1.07	4
18	0.05	2.94	1.64	10.65	127.3	1.05	4
19	0.08	4.10	2.31	14.46	127.3	1.07	4
20	0.10	5.18	2.94	17.84	127.3	1.07	4
21	0.10	5.18	2.94	17.84	222.8	1.05	4
22	0.13	6.19	3.53	20.91	159.2	1.07	4
23	0.10	6.83	2.94	17.84	495.2	1.01	8
24	0.15	7.16	4.10	23.72	159.2	1.07	4
25	0.15	7.16	4.10	23.72	127.3	1.05	4
26	0.20	5.18	5.18	28.75	143.2	1.07	4
27	0.20	5.18	5.18	28.75	127.3	1.05	4
28	0.15	9.39	4.10	23.72	117.0	1.01	8
29	0.25	10.65	6.19	33.15	39.8	1.07	4
30	0.25	10.65	6.19	33.15	12.7	1.05	4
31	0.30	12.24	7.16	37.04	82.8	1.07	4
32	0.30	12.24	7.16	37.04	57.3	1.05	4
33	0.35	13.74	8.08	40.52	82.8	1.07	4
34	0.35	13.74	8.08	40.52	82.8	1.05	4
35	0.40	15.16	8.97	43.64	70.0	1.07	4
36	0.40	15.16	8.97	43.64	95.5	1.05	4
37	0.20	15.16	5.18	28.75	12.7	1.07	16
38	0.20	15.16	5.18	28.75	22.3	1.07	16
39	0.45	16.53	9.82	46.44	82.8	1.07	4
40	0.45	16.53	9.82	46.44	55.7	1.05	4
41	0.50	17.84	10.65	48.97	54.1	1.07	4

Table 1 continued

No.	v_*	Ω_p	Ω_{\min}	Ω_{\max}	T_p	γ	k_p
42	0.50	17.84	10.65	48.97	63.7	1.05	4
43	0.55	19.10	11.46	51.24	71.6	1.05	4
44	0.60	20.31	12.24	53.29	79.6	1.07	4
45	0.40	24.78	8.97	43.64	19.1	1.07	16
46	0.50	28.75	10.65	48.97	15.6	1.07	16
47	0.50	28.75	10.65	48.97	95.5	1.07	16

Generation of a great volume of data was necessary, since the values of the β function have a considerable scatter. The one-point values of the real β_k^i and imaginary β_{-k}^i parts of the β function can be calculated through the Fourier coefficients for p_0 and η , viz.

$$\beta_k^i = \left| \eta_k^i \right|^{-2} \left(p_k^i \eta_k^i + p_{-k}^i \eta_{-k}^i \right), \tag{62a}$$

$$\beta_{-k}^i = \left| \eta_k^i \right|^{-2} \left(p_{-k}^i \eta_k^i - p_k^i \eta_{-k}^i \right), \tag{62b}$$

while the averaged values of β_k and β_{-k} were calculated in each bin using the root-mean-square method:

$$\beta_k = \sum_1^{N_i} \left(\left| \eta_k^i \right|^{-2} \left(p_k^i \eta_k^i - p_{-k}^i \eta_{-k}^i \right) \right) \left(\sum_1^{N_i} \left| \eta_k^i \right|^4 \right)^{-1}, \tag{63}$$

$$\beta_{-k} = \sum_1^{N_i} \left(\left| \eta_k^i \right|^{-2} \left(p_{-k}^i \eta_k^i - p_k^i \eta_{-k}^i \right) \right) \left(\sum_1^{N_i} \left| \eta_k^i \right|^4 \right)^{-1}, \tag{64}$$

where N_i is the number of points falling in each i th bin. The dispersion of the coefficients for the β function is calculated as follows

$$\sigma_k = \left(N_i^{-1} \sum_1^{N_i} \left(\beta_k^i \right)^2 - \beta_k^2 \right)^{1/2}, \tag{65a}$$

$$\sigma_{-k} = \left(N_i^{-1} \sum_1^{N_i} \left(\beta_{-k}^i \right)^2 - \beta_{-k}^2 \right)^{1/2}, \tag{65b}$$

where the β function (the vertical axis) as a function of Ω (the horizontal axis) is given in Fig. 7 for the three intervals: $-50 < \Omega < 50$, $-10 \leq \Omega \leq 10$ and $-2 < \Omega < 2$. The thick line (white in the left frame) corresponds to β_{-k} (taken with opposite sign), and the dashed line corresponds to β_k . As seen, the data on β have a very wide scatter, as if they were obtained experimentally, and it will be shown later that such a scatter has a deep physical nature. Still, the volume of the data is so large that the shape of the β function, especially for the range of $-20 \leq \Omega \leq 20$, can be determined with a satisfactory accuracy. The β function can be approximated through the following expressions

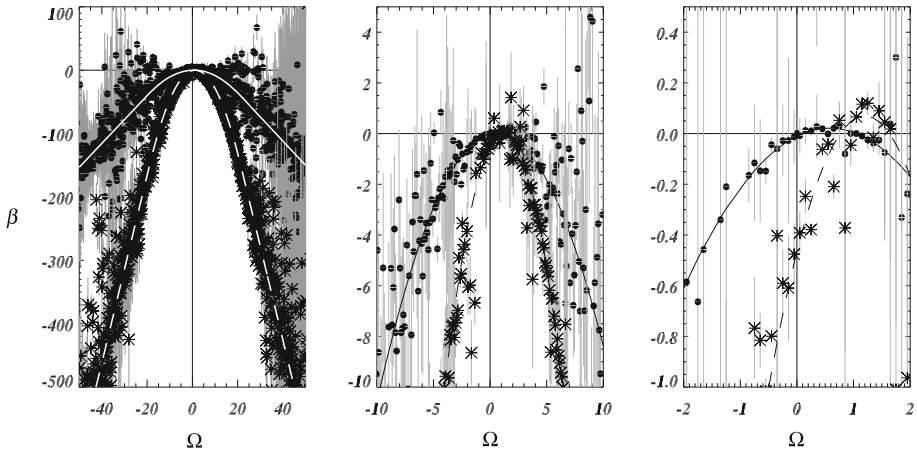


Fig. 7 The left frame— β (ordinate) as a function of Ω (abscissa). Thick lines (white—in the left frame) correspond to β_{-k} (taken with opposite sign), dashed line to β_k . The signs filled circle and asterisk indicate mean values in the bins for β_{-k} and β_k correspondingly, while grey lines are dispersion. The two other frames show the twice zoomed β function

$$\beta_{-k} = \begin{cases} b_1 + d_1 (\Omega - \Omega_1) & \Omega < \Omega_1 \\ b_0 + a_0 (\Omega - \Omega_0) + a_1 (\Omega - \Omega_0)^2 & \Omega_1 \geq \Omega < \Omega_2 \\ b_2 + d_2 (\Omega - \Omega_2) & \Omega \geq \Omega_2 \end{cases}, \quad (66a)$$

$$\beta_k = \begin{cases} b_3 + d_3 (\Omega - \Omega_4) & \Omega < \Omega_4 \\ b_4 + a_2 (\Omega - \Omega_3)^2 & \Omega_4 \geq \Omega < \Omega_5 \\ b_3 - d_3 (\Omega - \Omega_5) & \Omega > \Omega_5 \end{cases} \quad (66b)$$

where the numerical parameters are $\Omega_0 = 0.7, \Omega_1 = -19.3, \Omega_2 = 20.7, \Omega_3 = 1.2, \Omega_4 = -18.8, \Omega_5 = 21.2, a_0 = 0.02277, a_1 = 0.09476, a_2 = -0.3718, b_0 = -0.02, b_1 = 37.43, b_2 = 38.34, b_3 = -141.0, b_4 = 0.07, d_1 = -3.768, d_2 = 3.813, d_3 = 14.80$.

The β function is used for the calculation of the momentum \mathbf{F} and energy flux E in the spectral interval $\Delta\omega$

$$\mathbf{F}(\omega) = g\mathbf{k}\beta_{-k}(\Omega) S(\omega) \Delta\omega, \quad (67a)$$

$$E(\omega) = g\omega\beta_{-k}(\Omega) S(\omega) \Delta\omega \quad (67b)$$

where \mathbf{k} and ω are the *dimensional* wavenumber and frequency respectively, and S is the *dimensional* spectral density. The relations (67a,b) follow from the small-amplitude theory, and their applicability for the finite-amplitude waves was never discussed. Note that the equation for the spectral energy flux $E(\omega)$ is normally obtained from the equation for the spectral momentum flux $F(\omega)$ with the use of the dispersion relation $\omega = \sqrt{gk}$. For low wavenumbers the dispersion relation is valid, while for high frequency waves a connection between the wavenumber and wave frequency is actually absent (Chalikov 2005), hence, a flux of energy to the high-frequency waves should be a subject of a special investigation.

For validation of the β function the data obtained from the additional runs were used; these were carried out for various values of the initial steepness St defined as

$$St = \left(\sum_1^M k^2 |\eta_k|^2 \right)^{1/2}, \quad (68)$$

noting that in general St cannot serve as an indicator of steepness, since the integral of $k^2 S$ diverges at $S \sim \omega^{-5}$, thus, the value of St depends on the cut-off frequency. Here we use the parameter St only for comparison of different runs. All in all, 396 runs with the value of St varying within the range of 0.005–0.15, were used for the calculations. A non-dimensional root-mean-square error of pressure calculated through the β function p_b , as compared to the pressure calculated with use of the model, was obtained. The error is normalized by the dispersion of anomalies of the ‘true’ (i.e., p_0) pressure

$$e_1 = \frac{|p_0 - p_b|}{(\overline{p_0 - p_0})^{1/2}}. \quad (69)$$

The error increases from $e_1 = 0.3$ at $St = 0.01$ to $e_1 = 0.6$ at $St = 0.12$, then decreases, since dispersion of the pressure grows faster than the error. A good agreement between the ‘true’ pressure and the pressure restored with the use of the β function exists only for small and medium steepnesses. For the medium steepness $St = 0.1$ the correlation between p_0 and p_b is about 0.7, which makes the method of the flux calculation (67) still acceptable. For higher steepness the connection between the ‘true’ and ‘restored’ pressure actually disappears. There exist many reasons that explain why the method based on the β function cannot provide a good accuracy for the surface pressure calculations at higher steepness. The main reason is the non-linear dependence of pressure anomalies on steepness. This effect is clearly seen from the point-to-point comparison of p_0 and p_b given in Fig. 8 for various steepnesses. As seen, for steepness $St \sim 0.01$ the agreement between p_0 and p_b can be considered as good. For steepness $St = 0.05$ small pressure anomalies are still reproduced well, while large anomalies are underestimated. With a further increase of steepness a disagreement between the big values of p_0 and p_b becomes more significant. Such an effect can be easily explained. Large pressure anomalies are usually concentrated in the narrow zones in the vicinity of sharp peaks. Such a distribution of pressure does not have a clear spectral presentation; hence, the linear dependence (59) becomes inapplicable. As a result, the steep and sharp waves provide the flux of momentum and energy greatly exceeding the values that can be obtained on the basis of the linear dependence of pressure on elevation. The simulated growth of the flux of momentum occurs much faster with increase of the slope, as compared with the growth of the flux of momentum calculated on the basis of the β function. Such properties are well pronounced in the spectrum of wave drag in Fig. 9 where the pressure spectra are shown for different integral steepnesses. As seen, for the small and moderate steepness $St = 0.01$ – 0.05 the agreement between spectra for p_0 and p_b is good, while for high steepness $St = 0.13$ the spectrum density for p_0 is higher than the spectral density for p_b over the entire spectral interval.

10 The 1-D Model of the Wave Boundary Layer

2-D coupled modelling is a complicated problem that requires powerful computers. In this connection, it would make sense to develop the 1-D model that could describe the main

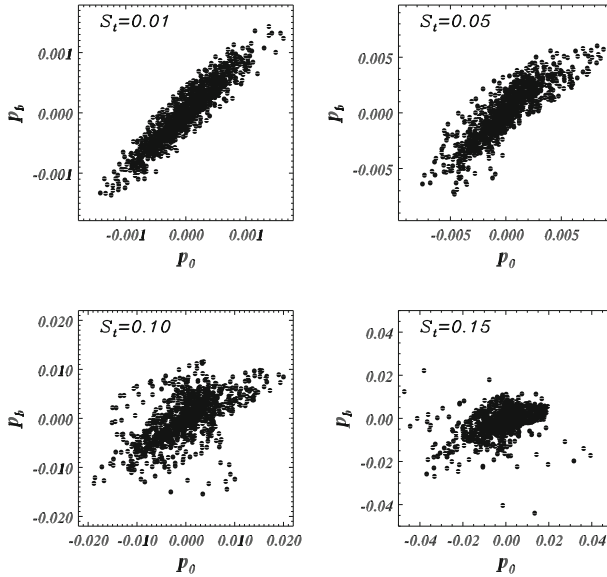


Fig. 8 The point-to-point comparison of surface pressure p_b calculated on the basis of the β function, with surface pressure p_0 calculated with the use of the 2-D coupled model for different integral steepness S_t

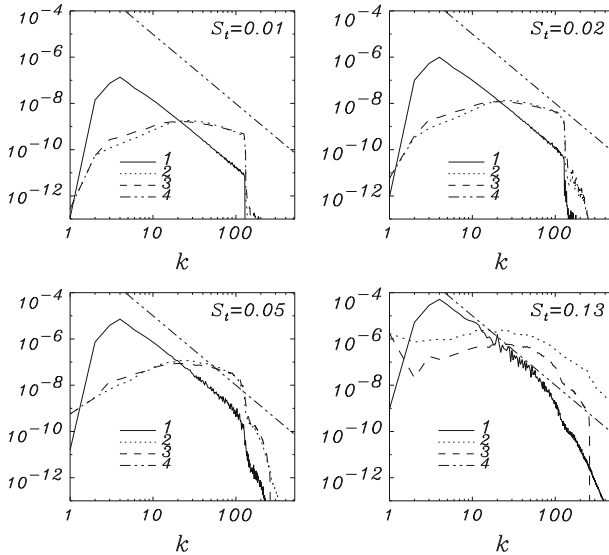


Fig. 9 Curve 1—wave spectrum; curve 2—surface pressure spectrum calculated using the coupled model; curve 3—surface pressure calculated with the use of β function for different integral steepness; curve 4 corresponds to the dependence k^{-3} (ω^{-5}). Steepness is indicated in each frame

features of the WBL suitable for different practical purposes. Such models were developed in Chalikov and Belevich (1993) and Chalikov (1995). The new data obtained with use of the 2-D coupled model allow a more precise formulation of this problem.

All variables in this section are assumed as dimensional. Neglecting the correlations of J , ξ_x with any dynamic characteristics, and taking into account that $\langle \zeta \rangle = z$, the one-dimensional equations of the WBL can be obtained by averaging Eqs. 5a and 16a,b along the coordinate ξ (the sign of averaging $\langle \cdot \rangle$ for all the variables being omitted)

$$\frac{\partial u}{\partial t} = \frac{\partial}{\partial z} \left(K \frac{\partial u}{\partial z} + \tau_w \right), \tag{70}$$

$$\frac{\partial e}{\partial t} = \frac{\partial}{\partial z} K_e \frac{\partial e}{\partial z} + P - \varepsilon, \tag{71}$$

$$\frac{\partial \varepsilon}{\partial t} = \frac{\partial}{\partial z} K_\varepsilon \frac{\partial \varepsilon}{\partial z} + \frac{\varepsilon}{e} (c_2 P - c_4 \varepsilon), \tag{72}$$

where $K = c_k e^2 / \varepsilon$ is the coefficient of the turbulent viscosity, P is the rate of production of the turbulent kinetic energy

$$P = \frac{\partial u}{\partial z} \left(K \frac{\partial u}{\partial z} + \tau_w \right), \tag{73}$$

τ_w is the flux of momentum produced by the wave-produced fluctuations of velocity, stresses and pressure (terms I, II and III in Eq. 54). According to Eq. 57 τ_w can be calculated by integration of the WPMF spectral constituencies

$$\tau_w = \int_0^{\omega_r} \tau_w^k \exp(-G(\bar{\omega})kz) dk, \tag{74}$$

where $G(\bar{\omega})$ is defined by Eq. 58, and the Fourier component of the WPMF on the surface τ_w^k is defined through the following expression

$$\tau_w^k = kg\beta_{-k} \left(\tilde{\Omega}_k \right) S(k), \tag{75}$$

where β_{-k} is defined in (66a), $\tilde{\Omega}_k = \omega u (\lambda_k/2) \cos \theta / g$ is the apparent frequency $S(k) = 0.5 (h_k^2 + h_{-k}^2)$ is the wavenumber spectrum. Also, $u (\lambda_\omega/2)$ is wind speed defined at $z = \lambda_\omega/2$, where $\lambda_\omega = 2\pi g / \omega^2$. The values of $u (\lambda_\omega/2)$ were calculated using the log-linear interpolation from $u (z)$ profiles. For the low wavenumber modes the height $\lambda_\omega/2$ often exceeds H_a , and the value of $u (\lambda_\omega/2)$ was calculated using the log-linear extrapolation that was used for $\omega < \omega_p$ only.

The stationary numerical solution for Eqs. 71–73 was obtained using the second-order scheme at the stretched grid with stretching coefficient $\gamma = 1.07$, and the explicit time scheme. The whole scheme requires a very small timestep $\Delta t \sim 10^{-3}$ s estimated through the following relation:

$$\Delta t = 0.25 \min \left(\frac{(\Delta z)^2}{K} \right). \tag{76}$$

For the stationary solution, the condition $\tau_z = K \partial u / \partial z + \tau_w = \tau$ must be satisfied over the entire WBL. The criterion for reaching the stationary solution was taken in the following form

$$(\max(\tau_z) - \min(\tau_z)) / \tau < 0.01, \tag{77}$$

and since a single run is simulated readily, a more efficient scheme was not used. However, for regular use of the 1-D model (for example, in the framework of a wave forecasting model), a better scheme must be semi-implicit, e.g. based on the TDMA scheme and iterations.

The boundary conditions for the 1-D equations are similar to those for the 2-D equations (Eqs. 17–20). At the upper boundary $z = H_a = 10H_s$ (H_s is the significant wave height) the tangential stress is assigned as

$$K \frac{\partial u}{\partial z} \Big|_{z=H_a} = \tau. \tag{78}$$

The rate of production P_H at the upper boundary of the domain $z = H_a$ is calculated as follows

$$P_H = \frac{v_*^3}{\kappa H_a} \tag{79}$$

($v_* = \tau^{1/2}$ is the friction velocity at $z = H_a$), while the energy of turbulence e and the rate of dissipation ε assume the following values

$$e_H = c_1 v_*^2, \tag{80a}$$

$$\varepsilon_H = \frac{v_*^3}{\kappa H_a}. \tag{80b}$$

The vertical diffusion of the turbulent energy $K_e \frac{\partial e}{\partial \zeta}$ at $z = 0$, as well as at the upper boundary of the domain, $z = H_a$, is equal to zero. The vertical diffusion of the dissipation rate at $z = 0$ and at $z = H_a$ is accordingly equal to

$$K_\varepsilon \frac{\partial \varepsilon}{\partial \zeta} (\zeta = 0) = -v_{s0}^4 z_1^{-1} c_3^{-1}, \tag{81a}$$

$$K_\varepsilon \frac{\partial \varepsilon}{\partial \zeta} (\zeta = H_a) = -v_*^4 H_a^{-1} c_3^{-1}, \tag{81b}$$

where $v_{s0} = \tau_0^{1/2}$ is the local tangential friction velocity defined by the local turbulent tangential stress at the interface τ_0 . The constants κ, c_1, c_3 , as well as the relationship between K, K_e, K_ε , are given in Sect. 2.

The 1-D WBL model is much simpler than the coupled 2-D model. Therefore, the wave spectrum can be extended up to high wavenumbers. The highest wavenumber ω_r is limited by the upper bounds of the non-dimensional frequency $\Omega = \pm 50$ in approximation (66a,b). It was assumed that at the horizontal scales of the order of the limit resolution g/ω_r^2 , sea surface can be considered as a smooth surface, so the local roughness parameter z_{0l} can be taken in the form (Monin and Yaglom 1971)

$$z_{0l} = 0.1\nu/v_{0z}, \tag{82a}$$

$$v_{0z} = \tau_0^{1/2}, \tag{82b}$$

where $\nu = 0.15 \times 10^{-4} \text{ m}^2 \text{ s}^{-1}$ is the molecular kinematic viscosity, v_{0z} is the local friction velocity, and τ_0 is the local tangential stress defined by Eq. 15 with use of the drag coefficient: $C_l = (k/\ln(\Delta z_1/z_{0l}))^2$, where the thickness of the lowest level Δz_1 is equal to $2z_\nu$ ($z_\nu = 60\nu/v_*$ is the height of the viscous sub-layer).

The initial 1-D wave spectrum was assigned by Eqs. 40–46, and the 2-D spectrum $S_2(\omega, \theta)$ was calculated as

$$S_2(\omega, \theta) = S(\omega) \psi(\theta), \tag{83}$$

where θ is the angle between the wind direction and the direction of a wave mode. The function ψ was taken in the form (Donelan 1990)

$$\psi = \psi_0^{-1} (\sec hb)^n, \quad (84a)$$

where

$$b = \begin{cases} 2.61\Omega_p^{1/3}, & \Omega_p < 0.95 \\ 2.28\Omega_p^{-1/3}, & \Omega_p > 0.95 \end{cases} \quad (84b)$$

and where ψ_0 is the normalizing factor. Note that the value of n is not well known even for a simple situation of the homogeneous wave field developed by a constant wind. For our calculation the value $n = 2$ corresponding to quite a broad spectrum, was chosen (Donelan 1990). Spectrum $S_2(\omega, \theta)$ can be fixed; however, in our calculations the spectrum was updated every 100 sec using a new value of Ω_{10} (Eq. 42) to obtain the fully adjusted WBL and wave field. The wave spectrum was approximated on the stretched grid over frequency (ω) $\Delta\omega_{i+1} = \gamma \Delta\omega_i$, with the stretching coefficient $\gamma = 1.03$. To approximate the low-frequency part of the spectrum the first frequency step $\Delta\omega_1$ was equal to $0.1\omega_p$ (ω_p is the dimensional peak frequency). The angle resolution $\Delta\theta$ equals 4° .

11 The 1-D Structure of the Wave Boundary Layer

The specific feature of the WBL is that the new mechanism of momentum transfer develops close to the surface (see Figs. 5, 6). The main advantage of the 1-D approach is that the wave drag formation can be considered in a wide range including the high frequencies. Contrary to the purely turbulent stress, the WPMF emerges due to the direct influence of waves, i.e. due to curvilinearity of the underlying surface. Since the total momentum flux must be constant over height for the steady wind, the turbulent momentum flux decreases when approaching the surface. Hence, the WPMF modifies the interconnection of the wind profile and the stress. Therefore, the structure of the WBL becomes different from that of the boundary layer above the flat surface. For investigation of the WBL structure on the basis of the 1-D model a series of calculations was carried out for $\Omega_p = (0.855, 1.0, 1.25, 1.5, 2.0, 3.0, 5.0)$ and for the initial value of u_{10} varying for each Ω_p within the interval 8–40 m s⁻¹. The initial conditions for the WBL were assigned in the same way as for the logarithmic boundary layer above the flat surface. Due to the appearance of wave drag in the process of reaching the equilibrium solution, the wind speed u_{10} decreases, while the final values of u_{10} become lower as compared to the initially assigned values.

Wind profiles above waves of different age for the two values of the wind speed u_{10} (about 15 and 30 m s⁻¹) are shown in Fig. 10 as a function of the dimensional height z (m). The thin lines indicate a downward extrapolation of the logarithmic wind profile from the levels where the WPMF equals zero, while the boundary layer preserves its standard structure. As seen, in the lowest part of the WBL a deviation of the wind profile from the logarithmic form can reach several m for $u_{10} \approx 14$ m s⁻¹, and 10 m for $u_{10} \approx 30$ m s⁻¹. It is quite important to note that such an effect takes place in the vicinity of the wave surface at heights of the order of a wave height. Such features can be investigated experimentally using the surface-following measurement technique similar to that designed by Donelan et al. (2006).

The most obscure problem of the wind–wave interaction is the dependence of stress on wind speed, traditionally represented as the dependence of the drag coefficient C_{10} on u_{10} . It is well known that the experimental data on C_{10} have a large scatter providing that C_{10} grows

Fig. 10 Wind profiles. In each group *thick curves* correspond to the values $U_{10}/c_p = 0.855, 1.0, 1.25, 1.5, 2.0, 3.0$. For the *left group* $13.4 < U_{10} < 15.4 \text{ m s}^{-1}$, whilst for the *right group*— $29.5 < U_{10} < 36.3 \text{ m s}^{-1}$. *Thin lines* correspond to logarithmic wind profiles extrapolated downward from the outside part of the WBL

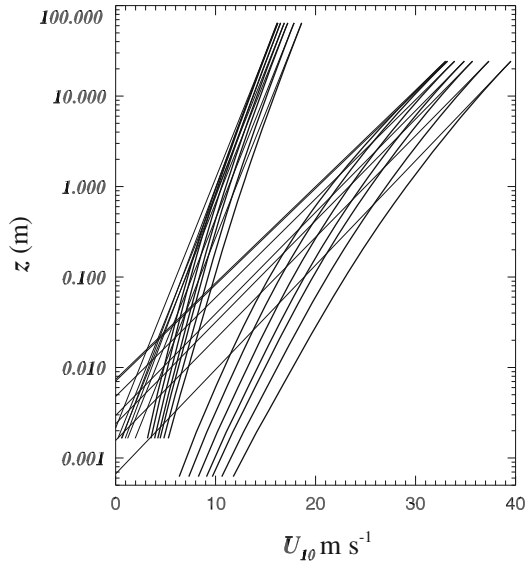
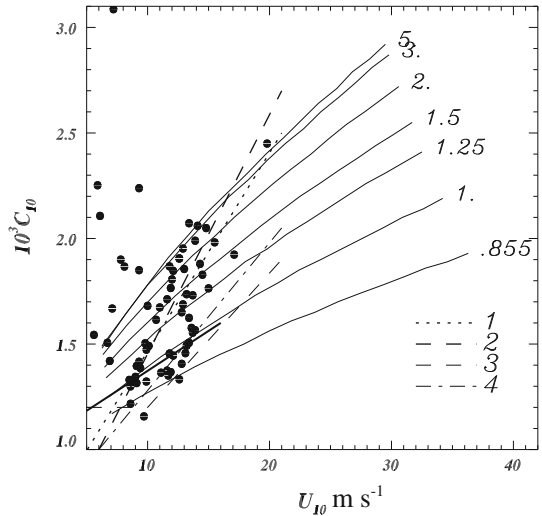


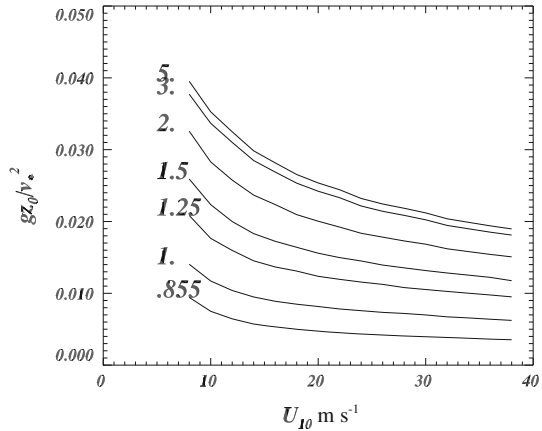
Fig. 11 The drag coefficient C_{10} as a function of U_{10} and $\Omega_p = U_{10}/c_p$ (curves labeled with Ω_p). Selection of C_d versus U_{10} dependences by other authors are shown: *Dots* are after Babanin et al. (2001); *bold line* is after Donelan (1982); *1* is after Geernaert et al. (1986); *2* is after Smith and Banke (1975); *3* is after Large and Pond (1982); *4* is after Yelland and Taylor (1996)



with wind speed at least up to $u_{10} = 25\text{--}30 \text{ m s}^{-1}$. The dependence of C_{10} on the wind speed and wave age calculated with use of the 1-D model is shown in Fig. 11. As seen, the drag coefficient depends rather on wave age than on wind speed. This conclusion is in qualitative agreement with observations (Smedman et al. 2003), and accounts for a wide scatter of the experimental data on the drag coefficient as a function of u_{10} , only.

The data on C_{10} and u_{10} can be interpreted in terms of the total roughness parameter z_0 based on all drag mechanisms. The dependence of the non-dimensional roughness $z_0 g/v_*^2$ is given in Fig. 12. The data do not prove a universal character of the scaling $Ch = v_*^2/g$ (Ch is the Charnock scale). However, the real data in the space (u_{10}, Ω_p) are distributed over a narrower area as compared with the area shown in Fig. 12. For example, only few data fall in the domain $u_{10} > 20, \Omega_p > 2$. Such events occur only at the early stages of

Fig. 12 The non-dimensional roughness parameter z_0g/v_*^2 as a function of U_{10} and Ω_p



wave development at medium and strong winds. Hence, the value of z_0g/v_*^2 varies within the range of 0.01-0.02, which is in good agreement with the values obtained by [Smith and Banke \(1975\)](#), [Garratt \(1977\)](#) and [Wu \(1980\)](#).

Let us consider the integral fluxes of momentum and energy to waves:

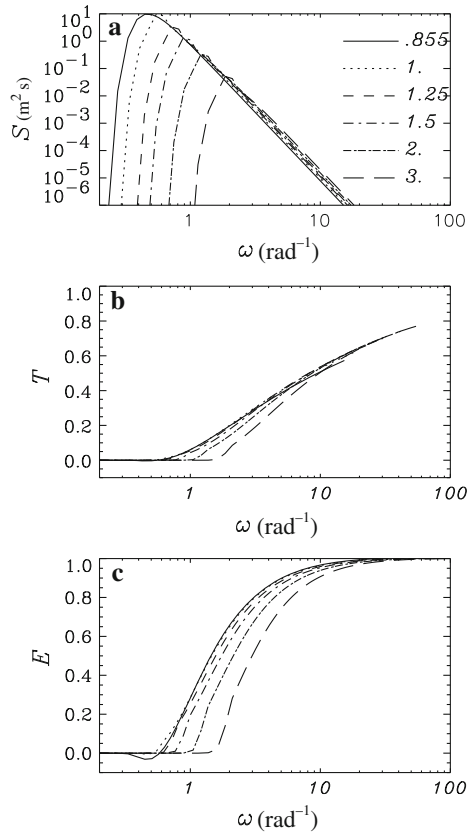
$$T(k) = \frac{g}{\tau} \int_0^k k\beta_{-k} S(k) dk, \tag{85}$$

$$E(k) = \frac{g}{E_{10}} \int_0^k \omega\beta_{-k} S(k) dk, \quad E_M = E(M), \tag{86}$$

where $E_{10} = \tau_{10}u_{10}$ is the downward flux of energy at $z = 10$ m. Equation 85 indicates the part of the total flux of momentum τ transferred to waves within the wavenumber range 0 to k . The integral spectra for T and E are shown in Fig. 13 (frames b, c) along with the wave spectrum (panel a). As seen, with increase of the wavenumber, the energy flux approaches the saturation level quite rapidly. It is different for the integral momentum flux, as it continues to grow with increase of frequency for all values of Ω_p . It is impossible to extend the spectrum to higher frequencies, as the β function was studied within the range of $-50 < \Omega < 50$. The data shown in panel b of Fig. 13 demonstrates that the flux of momentum is accumulated mostly in the high-frequency (high wavenumber) range of the spectrum. The explicitly reproduced momentum flux grows with increase in the cut-off wavenumber. The ratio of the calculated momentum flux to waves, and the total momentum flux is shown in Fig. 14, panel a. As seen, the momentum flux τ_w to waves can amount to 80% of the total momentum flux; and τ_w decreases with growth of Ω_p . It is interesting to note that the ratio of the energy flux to waves and the energy $E = \tau_{10}u_{10}$ transferred downward through $z = 10$ m exhibits quite an opposite behaviour: it increases with the growth of Ω_p . Such properties of momentum and energy exchange can be explained by the properties of the spectrum: the high-frequency spectral density responsible for the momentum flux is high for the young sea (an overshoot effect), while the low-frequency waves absorbing the major part of energy input, are larger for the old sea.

There is a possibility that in the smooth areas of a water surface some part of the momentum is transferred by molecular viscosity, while in the areas of high energy of short waves

Fig. 13 **a** Wave spectrum, **b** integral flux of momentum $T(k)$ (Eq. 85), **c** integral flux of energy $E(k)$ (Eq. 86) as functions of ω for different Ω_p

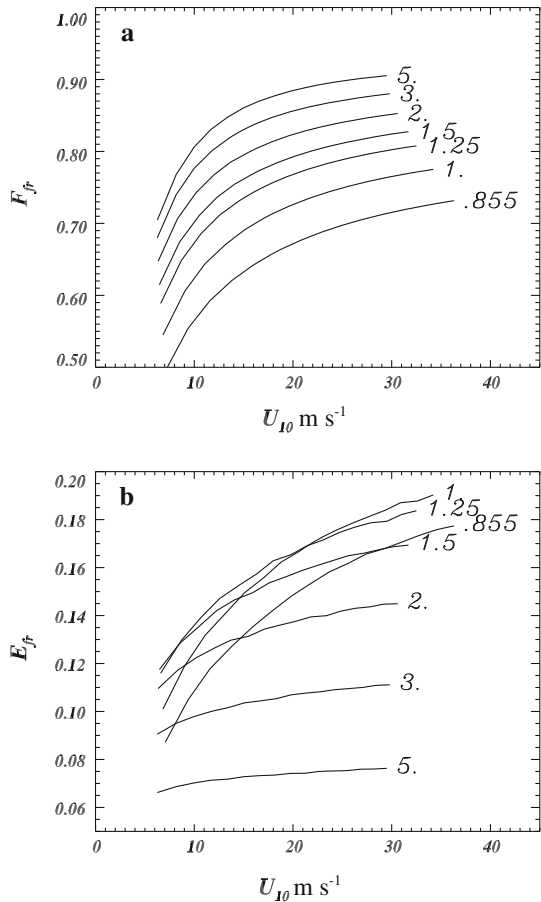


momentum is transferred to the small waves. Since the shape of the spectrum and β function at high frequencies are not known, it is impossible to investigate the ultimate ratio of the surface WPMF and the total surface stress. Fortunately enough, this problem is of no practical importance. The high-frequency waves quickly disappear (Chalikov 2005) thus transferring momentum to currents, while energy is transferred both to currents and turbulence (Chalikov and Belevich 1993). The most important thing is that the total friction on the wave surface depends significantly on wave energy at high frequencies (see Fig. 13, panel b). Most probably, the momentum flux and the drag coefficient also depend on the angle distribution of waves.

12 Drag Coefficient at High Wind Speed

As demonstrated in Fig. 11, the current theory predicts a monotonic growth of the drag coefficient with increase of wind speed. However, there exist some data revealing that for the wind speed exceeding 25–30 m s⁻¹, the drag coefficient reaches an upper limit (Powell et al. 2003; Donelan et al. 2004), while for further increase in wind speed the drag coefficient can even decrease. Earlier, such an effect was also noted when analyzing tropical cyclone development (Emanuel 1995). Currently some attempts are made to explain such behaviour of the drug coefficient on the basis of the ‘droplet theory’ (Andreas 2004; Kudryavtsev 2006). According

Fig. 14 **a** The ratio of surface WPMF and total stress τ as a function of U_{10} and U_{10}/c_p , **b** ratio of energy flux to waves and total energy flux transferred downward at $z = 10$ m (Eqs. 85, 86)

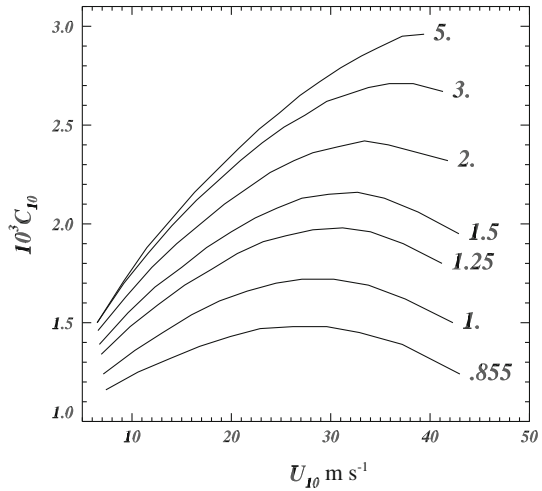


to the theory, the drops generated as a result of splitting of falling water volumes intensify the dissipation of turbulence, which causes a reduction of the drag coefficient. Such a scheme looks reasonable, although the model of the drop generation (as well as the mechanism of drops-turbulence interaction) uses too many arbitrary assumptions.

According to our data, the effect of the wave-drag reduction at high wind speeds can be easily explained through the influence of high-frequency waves. It would be appropriate to suggest that the energy of short waves at high winds decreases due to two factors: the presence of foam that suppresses short waves, and flow deceleration in troughs due to flow separation. The latter can be investigated using the coupled wind-wave model directly, though the model must take into account a broad range of the wave spectrum from peak waves to capillary waves. A high wind speed and the necessity to use a high vertical resolution in the WBL make this problem quite time consuming; anyway, such calculations are possible from the technical point of view.

Note that a reduction in the drag can also be caused by the ‘blowing away’ of sharp crests: high winds can smooth the surface and remove the elements responsible for stress. This effect was directly observed in the wind-wave tunnel (J. Troitskaya, private communication, 2010).

Fig. 15 The drag coefficient C_{10} as a function of U_{10} and $\Omega_p = U_{10}/c_p$ (15 curves labeled), taking into account the suppression of high-frequency modes



To prove that the reduction in the drag coefficient is caused by the suppression of small waves, the additional calculations of the drag coefficient were performed with use of the modified JONSWAP spectrum. A somewhat arbitrary assumption suggests that waves, whose frequency exceeds some value of ω_f , are absent. In our calculations the longest removed waves are 100 times shorter than the peak wavelength. The spectral density at $\omega = \omega_f$ equals $10^{-5} S_p$ (S_p is the spectral density at the wave peak). The amplitudes of such waves is about 100 times smaller than the amplitude of the dominant wave. Hence, the modifications of the spectrum are quite insignificant. The above modifications were introduced into a new series of the calculations with use of the 1-D model, Eqs. 73–77. The dependence of the drag coefficient (small waves being removed) on wind speed u_{10} is shown in Fig. 15. As seen, the drag coefficient significantly decreases at high wind speed; for a developed sea ($\Omega_p \sim 1$) the drag coefficient C_{10} has the maximum of $C_{10} \approx 1.5 \times 10^{-3}$ at $u_{10} \approx 30 \text{ m s}^{-1}$, while for the younger waves the maximum is shifted to higher wind speeds.

It should be emphasized that the result presented in Fig. 15 is purely qualitative, since the exact shape of the spectrum is unknown at high wind speeds. Figure 15 just illustrates a simple explanation of the drag coefficient reduction at high wind speeds on the basis of the high-frequency wave spectrum modification.

13 Conclusions

We describe the first attempts to simulate a wind and wave interaction process on the basis of a coupled wind–wave model. Both parts of the model are written in conformal surface-following coordinates. The use of such coordinates is the only way to construct an efficient two-dimensional coupled model since conformity allows considerable simplifications in the formulation of the problem and the numerical scheme. Contrary to all previous investigations, the problem of the wind–wave interaction is formulated as a statistical fluid dynamics problem, and the coupled model used for the simulation of a statistical regime of flows.

The coupled model based on the full equations is used for the simulation of an evolution of a multi-mode wave field under the action of wind. Such calculations cannot be carried out without the introduction of the new physics into a wave model. Firstly, a flux of energy in a

subgrid part of the spectrum was parameterized by selective smoothing (Eqs. 36, 37). Without such smoothing the calculations terminate due to the non-linear instability. Secondly, it was necessary to prevent overturning of waves, which was parameterized by the introduction of a ‘breaking’ algorithm representing highly selective local smoothing of the surface and a surface potential in separate intervals in physical space where a high profile curvature is observed (Eq. 38a,b). Both of the smoothing algorithms are widely used in geophysical fluid dynamics. In particular, a breaking parameterization is very similar to that of the static instability in numerical atmospheric models.

A closure problem for Reynolds equations is a subject of numerous speculations. It is well-known that the closed system of the Keller–Friedmann equation (Keller and Friedmann 1924) cannot be derived formally (see Monin and Yaglom 1971). Therefore, many additional assumptions have been introduced since. Applicability of the closed equations can be proved by comparison with the experimental data only. A simple $K - \varepsilon$ scheme was used in the model. Contrary to the conclusions of Belcher et al. (1994) made within the framework of the linear approach, we could hardly find solid arguments in favour of the use of a more complex scheme. It would be naive to expect that the introduction of more equations containing many poorly known constants could lead to a substantial improvement of the results. Experience shows that the straightforward approach used in the present work, is superior to a complex approach.

The surface-following coordinates allow introducing explicit expressions for different mechanisms of the momentum (and energy) fluxes produced by the averaged and fluctuating turbulence as well as by velocity and pressure fields (Fig. 5). The sum of the above fluxes is the so-called wave produced momentum flux (WPMF) that plays an important role in construction of a simplified 1-D model of the WBL (Fig. 6).

The instantaneous boundary-layer fields are highly chaotic, although after appropriate averaging they reveal a simple regularity: a vertical distribution of the Fourier modes for pressure, kinetic energy and other variables are clearly stratified over wavenumbers.

The obtained data allow evaluation of the so-called β function, i.e., a complex coefficient in Eq. 59. The data on the β function exhibit wide scatter, but since the volume of data is big enough (about 1,400,000 points), the shape of the β function was defined with satisfactory accuracy up to high non-dimensional frequencies (Eqs. 66a,b; Fig. 7). The main reason for wide scatter is not an accuracy of modeling, but rather a result of the non-linearity of the flow. The interaction of wind and waves generates a much broader pressure spectrum than can be reproduced using the linear wave generation theory (Figs. 8, 9).

The vertical profiles of Fourier components for the WPMF normalized by a surface value can be represented as a function of a non-dimensional height kz , which is used in construction of the 1-D WBL model. If the number of wave modes taken into account is large enough, the WPMF on a surface approaches the value of the total stress (which due to assumed steadiness is equal to the value of the outer stress). However, contrary to suggestion of Janssen (1991), the ultimate proportion of form and tangential stresses cannot be determined, because the WPMF is a function of height, as well as of vertical and spectral resolution (see Chalikov 1993). When the number of wave modes is not large, the influence of form drag due to subgrid waves should be taken into account with the use of an appropriate value of the local drag coefficient. Hence, when waves are described directly, a drag coefficient should be considered as a spectral concept.

Unlike turbulent friction, the WPMF is not an internal property of a turbulent boundary layer since it is created by external forcing, i.e., by waves. The presence of the WPMF brings forward the specific features of the WBL, e.g. the wind profile in the lowest part of the WBL deviates considerably from the logarithmic form (Fig. 10). The 1-D theory of the WBL allows

investigation of the dependence of the drag coefficient C_{10} on the wind speed u_{10} (Fig. 11). It is suggested that the wide scatter in the experimental data on C_{10} can be explained by an additional dependence on the wave spectrum shape. The same effect is clearly pronounced in a roughness parameter normalized by the Charnock scale (Fig. 12). Evidently, the drag coefficient can depend also on other parameters: the broadness of the wind spectrum, wind gustiness and stratification (when the air–sea temperature difference is large).

The main part of the surface drag is concentrated in the high-frequency portion of the spectrum (Fig. 13), therefore, the ratio of the surface WPMF and the total stress is a function of the cut-off frequency. This is why the decrease of C_{10} at high winds can be easily explained by the influence of the wave energy density at high frequencies. To illustrate such an effect we assumed that high frequency waves become suppressed beyond some wavenumber ω_f . There exist several explanations for this effect. Despite the fact that ω_f is many times higher than the peak frequency ω_p , and that the energy of suppressed waves is very small, the effect of such surface smoothing is dramatic: starting with the wind speed of 25–30 m s⁻¹, the drag coefficient decreases in the same way as in observations (Fig. 15). Such results do not claim to be qualitatively accurate, but are an illustration of a potential mechanism for the drag coefficient reduction occurring in stormy conditions. A further investigation of the above effect must be focused on the energy of small waves and their distribution over the phases of large waves.

The current paper considers the problem of ocean–atmosphere interaction with allowance for surface waves. As a result of such investigations the atmospheric large-scale modelling (including weather forecast and climate simulation) may be improved through implementation of the essentially new physics. The current atmospheric and coupled models do not take into consideration a state of the ocean surface while a less important interaction of atmosphere and land is parameterized in more detail. The surface wave spectral modelling is not time consuming; thus, a wave model can be easily combined with the atmospheric and ocean models (see Chalikov and Belevich 1993). The one-dimensional model suggested in the current paper is designed for the linking of atmospheric and ocean models through a wave model.

Acknowledgements DC would like to thank his wife Olga for her assistance while preparing the manuscript for publication, as well as Dr. Babanin for a very useful discussion of the problems covered in the current article. The author also would like to thank the unknown reviewers for their valuable comments and suggestions.

References

- Andreas EL (2004) Spray stress revised. *J Phys Oceanogr* 34:1429–1440
- Babanin AV (2009) Breaking of ocean surface waves. *Acta Phys Slovaca* 594:305–335
- Babanin AV, Soloviev YP (1998) Investigation of transformation of the wind wave frequency spectrum with fetch and the stage of development. *J Phys Oceanogr* 28:563–576
- Babanin AV, Young IR, Banner ML (2001) Breaking probabilities for dominant surface waves on water of finite constant depth. *J Geophys Res* 106(C6):11659–11676
- Banner ML, Pierson WL (2007) Wave breaking onset and strength for two-dimensional and deep-water wave groups. *J Fluid Mech* 585:93–115
- Belcher S, Harris JA, Street RL (1994) Linear dynamics of wind waves in coupled turbulent air-flow. Part 1. Theory. *J Fluid Mech* 271:119–151
- Benjamin TB, Feir JE (1967) The disintegration of wave trains in deep water. *J Fluid Mech* 27:417–430
- Chalikov DV (1976) A mathematical model of wind-induced waves. *Dokl Acad Sci USSR* 229:121–126
- Chalikov DV (1978) Numerical simulation of wind–wave interaction. *J Fluid Mech* 87:561–582

- Chalikov DV (1986) Numerical simulation of the boundary layer above waves. *Boundary-Layer Meteorol* 34:63–98
- Chalikov D (1993) Comments on “Wave induced stress and the drag of air flow over sea waves” and “Quasi-linear theory of wind–wave generation applied to wave/forecasting”. *J Phys Oceanogr* 1(423):11597–11600
- Chalikov D (1995) The parameterization of the wave boundary layer. *J Phys Oceanogr* 25:1335–1349
- Chalikov D (1998) Interactive modelling of surface waves and boundary layer. *Ocean wave measurements and analysis*. ASCE. In: Proceedings of the third international symposium WAVES, vol 97, pp 1525–1540
- Chalikov D (2005) Statistical properties of nonlinear one-dimensional wave fields. *Nonlinear Process Geophys* 12:1–19
- Chalikov D (2007) Simulation of Benjamin–Feir instability and its consequences. *Phys Fluids* 19:016602–016615
- Chalikov D (2009) Freak waves: their occurrence and probability. *Phys Fluids* 21:076602. doi:[10.1063/1.3175713](https://doi.org/10.1063/1.3175713)
- Chalikov D, Belevich M (1993) One-dimensional theory of the wave boundary layer. *Boundary-Layer Meteorol* 63:65–96
- Chalikov D, Sheinin D (1996) Numerical modelling of surface waves based on principal equations of potential wave dynamics. Technical Note. NOAA/NCEP/OMB, 54 pp
- Chalikov D, Sheinin D (1998) Direct modelling of one-dimensional nonlinear potential waves. *Nonlinear ocean waves*. In: Perrie W (ed) *Advances in fluid mechanics*, vol 17. WIT Press, Southampton, pp 207–222
- Chalikov D, Sheinin D (2005) Modelling of extreme waves based on equations of potential flow with a free surface. *J Comput Phys* 210:247–273
- Crapper GD (1957) An exact solution for progressive capillary waves of arbitrary amplitude. *J Fluid Mech* 96:417–445
- Dold JW (1992) An efficient surface-integral algorithm applied to unsteady gravity waves. *J Comput Phys* 103:90–115
- Donelan MA (1982) The dependence of the aerodynamic drag coefficient on wave parameters. In: Proceedings of the first international conference on the meteorology and air–sea interaction in coastal zone, Hague, The Netherlands. American Meteorological Society, Boston, pp 381–387
- Donelan MA (1990) Air–sea interaction. In: LeMehaute B, Hanes DM (eds) *The sea: ocean engineering science*, vol 9. Wiley-Interscience, New York, pp 239–292
- Donelan MA, Haus BK, Reul N, Plant WJ, Stiassnie M, Graber HC, Brown OB, Saltzman ES (2004) On the limiting aerodynamic roughness of the ocean in very strong winds. *Geophys Res Lett* 31:L18306. doi:[10.1029/2004GL019460](https://doi.org/10.1029/2004GL019460)
- Donelan MA, Babanin AV, Young R, Banner ML (2006) Wave-follower field measurements of the wind-input spectral function. Part II: Parameterization of the wind input. *J Phys Oceanogr* 36:1672–1689
- Emanuel KA (1995) Sensitivity of tropical cyclones to surface exchange coefficients and a revised steady-state model incorporating eye dynamics. *J Atmos Sci* 52:3969–3976
- Fornberg B (1980) A numerical method for conformal mapping. *SIAM J Sci Comput* 1:386–400
- Garratt JR (1977) Review of drag coefficient over oceans and continent. *Mon Weather Rev* 105:915
- Geernaert GL, Katsaros KB, Richter K (1986) Variation of the drag coefficient and its dependence on sea state. *J Geophys Res* 91(C6):7667–7679
- Gent PR, Taylor PA (1976) A numerical model of the air flow above water waves. *J Fluid Mech* 77:105–128
- Hasselmann K (1962) On the nonlinear energy transfer in a gravity wave spectrum. P.1. General theory. *J Fluid Mech* 12:481–500
- Janssen PAEM (1991) Quasi-linear theory of wind wave generation applied to wave forecasting. *J Phys Oceanogr* 21:1631–1642
- Kahma KK, Calkoen CJ (1992) Reconciling discrepancies in the observed growth of wind generated waves. *J Phys Oceanogr* 22:52–78
- Kano T, Nishida T (1979) Sur le ondes de surface de l’eau avec une justification mathematique des equations des ondes en eau peu profonde. *J Math Kyoto Univ (JMKYAZ)* 19-2:335–370
- Keller LV, Friedmann AA (1924) Differentialgleichung für die turbulente Bewegung einer kompressiblen Flüssigkeit. In: Proceedings of the 1st international congress for applied mechanics, vol 31, issue 4, pp 789–799
- Kudryavtsev VN (2006) On effect of sea drops on atmospheric boundary layer. *J Geophys Res* 111:C07020. doi:[10.1029/2005JC002970](https://doi.org/10.1029/2005JC002970)
- Large WG, Pond S (1982) Sensible and latent heat flux measurements over the ocean. *J Phys Oceanogr* 12:464–482
- Lauder BE, Spalding DB (1974) The numerical computation of turbulent flows. *Comput Methods Appl Mech Eng* 3:269–289

- Longuet-Higgins MS, Tanaka M (1997) On the crest instabilities of steep surface waves. *J Fluid Mech* 336:51–68
- Mastenbroek CV, Makin VK, Garrat MH, Giovanangeli JP (1996) Experimental evidence of the rapid distortion of the turbulence in the air flow over water waves. *J Fluid Mech* 318:273–302
- Miles JW (1957) On the generation of surface waves by shear flows. *J Fluid Mech* 3:185
- Monin AS, Yaglom AM (1971) *Statistical fluid mechanics: mechanics of turbulence*, vol 1. The MIT Press, Cambridge, 769 pp
- Orszag SA (1970) Transform method for calculation of vector coupled sums. Application to the spectral form of vorticity equation. *J Atmos Sci* 27:890–895
- Ovsyannikov LV (1973) *Dinamika sploshnoi sredy*, no 15. M.A. Lavrent'ev Institute of Hydrodynamics Sib Branch USSR Acad Sci, pp 104–125 (in Russian)
- Phillips OM (1977) *Dynamics of upper ocean*, 2nd edn. Cambridge University Press, Cambridge, 336 pp
- Powell MD, Vickery PJ, Reinhold TA (2003) Reduced drag coefficient for high wind speeds in tropical cyclones. *Nature* 422:279–283
- Sheinin D, Chalikov D (2005) Hydrodynamical modelling of potential surface waves. In: *Problems of hydro-meteorology and environment on the eve of XXI century*. In: Proceedings of international theoretical conference, St. Petersburg, June 24–25, 1999. Hydrometeoizdat, St. Petersburg, pp 305–337
- Simonov VV (1982) On the calculation of the drag of wavy surface. *Izv Atmos Ocean Phys* 18:269–275
- Smedman AS, Larsen XG, Höström U (2003) Is the logarithmic wind law valid over the sea? In: Sajjadi SG, Hunt JCR (eds) *Wind over waves II: forecasting and fundamentals of applications*. Horwood Publishing Ltd., Chichester
- Smith SD, Banke EG (1975) Variation of the sea surface drag coefficient with wind speed. *Q J Roy Meteorol Soc* 101:665
- Tanveer S (1991) Singularities in water waves and Rayleigh–Taylor instability. *Proc Roy Soc Lond A*435:137–158
- Tanveer S (1993) Singularities in the classical Rayleigh–Taylor flow: formation and subsequent motion. *Proc Roy Soc Lond A*441:501–525
- Tolman H, Chalikov D (1994) Development of a third-generation ocean wave model at NOAA-NMC. In: Isaacson M, Quick MC (eds) *Physical and numerical modeling*. University of British Columbia, Vancouver, pp 724–733
- Tolman H, Chalikov D (1996) On the source terms in a third-generation wind wave model. *J Phys Oceanogr* 26(11):2497–2518
- Wu J (1980) Wind-stress coefficient over sea surface near neutral conditions—a revisit. *J Phys Oceanogr* 10:727
- Yelland MJ, Taylor PK (1996) Wind stress measurements from the open ocean. *J Phys Oceanogr* 26:541–558
- Zakharov VE, Dyachenko AI, Vasilyev OA (2002) New method for numerical simulation of a nonstationary potential flow of incompressible fluid with a free surface. *Eur J Mech B* 21:283–291
- Zakharov VE, Dyachenko AI, Prokofiev AO (2006) Freak waves as nonlinear stage of Stokes wave modulation instability. *Eur J Mech B* 25:677–692